KEK/J-PARC-PAC 2011-27

# Letter of Intent for Phase-I of the COMET Experiment at J-PARC

March 11, 2012

# Executive Summary

We hereby express our interest to employ a staged approach for the construction of the COherent Muon to Electron Transition (COMET) experiment that will search for neutrinoless $\mu^- - e^-$ conversions with a single-event sensitivity of $3\times10^{-17}$. This sensitivity is a factor of 10,000 better than achieved by the SINDRUM-II experiment which set the current world's best limit for $\mu^- - e^-$ conversions. The COMET experiment was given Stage-1 approval, of two stages, by the J-PARC Program Advisory Committee in 2009 and given the experiment number J-PARC E21.

The proposed J-PARC mid-term plan includes the construction of the COMET beamline. This will provide the proton beamline for COMET and part of the muon beamline in the south area of the J-PARC Hadron Experimental Hall. We consider a staged approach for COMET as described below. To realise this approach we would like to construct the muon beamline up to the end of the first 90° bend in the muon beamline so that a muon beam can be extracted to the experimental area. We refer to this as "COMET Phase-I". In COMET Phase-I, we will:

1. make a direct measurement of the proton beam extinction and other potential background sources for the full COMET experiment, using the actual COMET beamline, and
2. carry out a search for $\mu^- - e^-$ conversion with a singe-event sensitivity of $3.1\times10^{-15}$, which is better than achieved by SINDRUM-II.

The direct measurement of potential background sources will be vital for the full COMET experiment. The current background estimates are made by extrapolating existing measurements over four orders of magnitude, and uncertainties are therefore difficult to quantify and are potentially large. However, once the partial muon beamline is completed, it will become possible to make realistic background estimations from direct measurements. Based on these, the final design of the COMET beamline and detectors will be optimised and uncertainties on the background estimations minimised. This will significantly enhance the ultimate sensitivity of the COMET experiment.

A search for $\mu^- - e^-$ conversion with a sensitivity beyond that achieved to date will be performed. The pion contamination in the muon beam at COMET Phase-I will be high because of the shorter muon beamline. However, since the muon intensity will be the highest in the world by several orders of magnitude, as for the full COMET experiment, we will be able to probe beyond the current limit and set the world's best limit should no signal be observed. The addition of the full muon beamline in Phase-II will give the ultimate sensitivity for the COMET experiment. The proposed staged approach will produce valuable scientific outcomes at each phase and the physics impact of our CLFV search in COMET Phase-I will be significant.

In summary, we have identified a strong physics case to stage the construction of the COMET experiment that is aligned with the proposed J-PARC mid-term plan for the construction of the COMET beamline. We are hoping to start the construction in 2013 and to carry out our measurements in 2016.

R. Akhmetshin, A. Bondar, L. Epshteyn, G. Fedotovich, D. Grigoriev, V. Kazanin,
A. Ryzhenenkov, D. Shemyakin, Yu. Yudin
*Budker Institute of Nuclear Physics (BINP), Novosibirsk, Russia*

Y.G. Cui, R. Palmer
*Department of Physics, Brookhaven National Laboratory, USA*

Y. Arimoto, K. Hasegawa, Y. Igarashi, M. Ikeno, S. Ishimoto, Y. Makida, S. Mihara,
T. Nakamoto, H. Nishiguchi, T. Ogitsu, C. Omori, N. Saito, K. Sasaki, M. Sugano,
Y. Takubo, M. Tanaka, M. Tomizawa, T. Uchida, A. Yamamoto, M. Yamanaka,
M. Yoshida, Y. Yoshii, K. Yoshimura
*High Energy Accelerator Research Organization (KEK), Tsukuba, Japan*

Yu. Bagaturia
*Ilia State University (ISU), Tbilisi, Georgia*

P. Dauncey, P. Dornan, B. Krikler, A. Kurup, J. Nash, J. Pasternak, Y. Uchida
*Imperial College London, UK*

P. Sarin, S. Umasankar
*Indian Institute of Technology Bonbay, India*

Y. Iwashita
*Institute for Chemical Research, Kyoto University, Kyoto, Japan*

V.V. Thuan
*Institute for Nuclear Science and Technology, Vietnam*

H.-B. Li, C. Wu, Y. Yuan
*Institute of High Energy Physics (IHEP), China*

A. Liparteliani, N. Mosulishvili, Yu. Tevzadze, I. Trekov, N. Tsverava
*Institute of High Energy Physics of I.Javakhishvili State University (HEPI TSU), Tbilisi, Georgia*

S. Dymov, P. Evtoukhovich, V. Kalinnikov, A. Khvedelidze, A. Kulikov,
G. Macharashvili, A. Moiseenko, B. Sabirov, V. Shmakova, Z. Tsmalaidze
*Joint Institute for Nuclear Research (JINR), Dubna, Russia*

M. Danilov, A. Drutskoy, V. Rusinov, E. Tarkovsky
*Institute for Theoretical and Experimental Physics (ITEP), Russia*

T. Ota
*Max-Planck-Institute for Physics (Werner-Heisenberg-Institute), Munchen, Germany*

Y. Mori, Y. Kuriyama, J.B. Lagrange
*Kyoto University Research Reactor Institute, Kyoto, Japan*

C.V. Tao
*College of Natural Science, National Vietnam University, Vietnam*

M. Aoki, T. Hiasa, I.H. Hasim T. Hayashi, Y. Hino, S. Hikida, T. Itahashi, S. Ito,
Y. Kuno*, T.H. Nam, H. Nakai, H. Sakamoto, A. Sato, N.D. Thong, N.M. Truong

*Osaka University, Osaka, Japan*

M. Koike, J. Sato
*Saitama University, Japan*

D. Bryman
*University of British Columbia, Vancouver, Canada*

S. Cook, R. D'Arcy, A. Edmonds, M. Lancaster, M. Wing
*University College London, UK*

E. Hungerford
*University of Houston, USA*

W.A. Tajuddin
*University of Malaya, Malaysia*

R.B. Appleby, W. Bertsche, M. Gersabeck, H. Owen, C. Parkes
*University of Manchester, UK*

F. Azfar
*University of Oxford, UK*

Md. Imam Hossain
*University Technology Malaysia*

T. Numao
*TRIUMF, Canada*

---

* Contact Person

# Contents

# Chapter 1

# Overview

## 1.1 Introduction

Charged lepton flavor violation (CLFV) has yet to be observed and is known to be sensitive to new physics beyond the Standard Model (SM), as discussed in Chapter 2. The J-PARC E21 experiment is an experiment to search for a CLFV process of neutrinoless muon-to-electron conversion ($\mu^-{-}e^-$ conversion) in a muonic atom,

$$\mu^- + N(A, Z) \to e^- + N(A, Z), \tag{1.1}$$

at a single-event sensitivity of $3 \times 10^{-17}$ at the Japanese Proton Accelerator Research Complex (J-PARC). This experiment is called COherent Muon to Electron Transition (COMET). This anticipated sensitivity goal of the COMET experiment is a factor of 10,000 better than that of the current experimental limit[1].

The COMET experiment is designed to be carried out in the Nuclear and Particle Experimental Hall (NP Hall) using a bunched proton beam that is slow-extracted from the J-PARC main ring (MR). The experimental set-up consists of the dedicated proton beam line, the muon beam section and the detector section. The muon beam section is composed of the pion capture solenoids with high magnetic field, and the muon transport with curved and straight solenoids. The detector section is composed of the muon stopping target, the electron transport for $\mu^-{-}e^-$ conversion signals, followed by the detector systems. A schematic drawing of the experimental set-up is shown in Fig. 1.1.

In order to improve the sensitivity by a factor of 10,000 over the current limit, several important features have been considered, such as

- a highly intense muon source,
- a pulsed proton beam with high proton extinction factor, and
- curved solenoids for charge and momentum selection.

The COMET experimental design has several advantages. These are mainly due to the C-shaped design of the muon transport and the electron transport:

- **C-shape muon transport in the muon beam**
  Instead of the S-shape that was adopted by MECO, the C-shape muon transport in the muon beam line (from the pion production to the muon-stopping target) is

---

[1] The present published limit is $B(\mu^- + \mathrm{Au} \to e^- + \mathrm{Au}) = 7 \times 10^{-13}$ from SINDRUM-II at PSI [1].

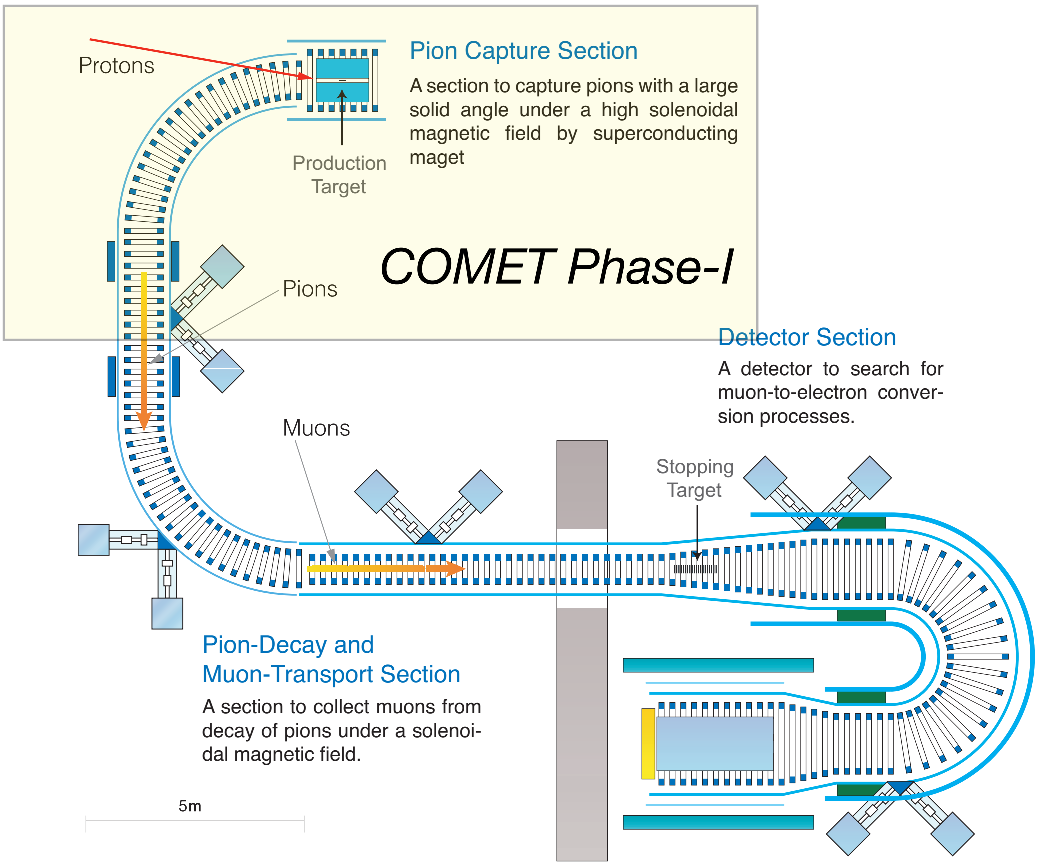

Figure 1.1: Schematic layout of COMET and COMET Phase-I

chosen in COMET. This requires an additional compensating dipole field, which can be produced using separate dipole coils or by tilting the solenoid coils. Since the muon momentum dispersion is proportional to a total bending angle, the C-shape beamline will produce a larger separation of the muon tracks as a function of momentum, resulting in improved momentum selection, which can also be varied independently of the solenoidal field if separate dipole coils are employed.

- **C-shape electron transport in the detector**
  Instead of a straight solenoid, a C-shaped electron transport (from the muon-stopping target to the detector) is adopted in the COMET spectrometer. The principle of momentum selection is the same as that used in the muon transport system, but, in the spectrometer, electrons of low momenta which mostly come from muon decay in orbit (DIO) are removed. As a result, the detector rate will be reduced significantly and the probability of false-tracking is highly suppressed. The tracking detector rate, including the direct hit of DIO electrons and secondary electrons from scattering and photon conversion, is expected to be less than 1 MHz. This is almost two orders of magnitudes less than the expected detector rate for the MECO experiment. Another advantage of using a curved solenoid for the electron transport is that it will eliminate the need for a proton absorber. Mu2e must shield their electron spectrometer from protons produced by the nuclear capture of

stopping muons, and therefore, COMET will have a better energy resolution. Also because of the suppression of low-energy particles, the detector geometry can be made simpler—as is the case with the present configuration with straw-chamber planes transverse to the field axis and an electron calorimeter whose front face is perpendicular to the field axis.

## 1.2 COMET Staged Approach and the J-PARC Mid-term Plan

The proposed J-PARC mid-term plan includes the construction of the COMET beam line. This will provide the proton beam line for COMET and part of the muon beam line in the south area of the J-PARC Hadron Experimental Hall. We consider a staged approach for COMET. To realize this staged approach, we would like to construct the COMET muon beam line up to the end of the first 90° bend so that a muon beam can be extracted to the experimental area. This stage is called "COMET Phase-I". Figure 1.1 shows the part of the muon beamline that will be constructed in COMET Phase-I.

COMET Phase-I has two major goals:

- direct measurement of the proton beam extinction factors and other potential background sources for the full COMET experiment by using the actual COMET beamline constructed at COMET Phase-I, and
- a search for $\mu^-{-}e^-$ conversion with a single-event sensitivity of better than $3.1 \times 10^{-15}$ which is a factor of 200 times better than the SINDRUM-II limit.

### 1.2.1 Direct background measurements

The direct measurement of potential background sources will be vital for the full COMET experiment. The current background estimates are made by extrapolating existing measurements over four orders of magnitude, and uncertainties are therefore difficult to quantify and are potentially large. However, once the partial muon beamline is completed, it will become possible to make realistic background estimations from direct measurements. Potential backgrounds that can be measured are pions, neutrons, antiprotons and electrons in the beam, and the electron spectrum of muon decays in orbit (DIO), and so on. To carry out these direct measurements, a dedicated detector with charged particle tracking and an electromagnetic calorimeter for direct background measurement will be prepared. Based on these, the final design of the COMET beamline and detectors will be optimised and uncertainties on the background estimations minimised. This will significantly enhance the ultimate sensitivity of the COMET experiment.

### 1.2.2 Search for $\mu^-{-}e^-$ conversion and other CLFV muon processes

A search for $\mu^-{-}e^-$ conversion with a single-event sensitivity beyond that achieved to date will be performed. This anticipated single-event sensitivity is about a factor of 200 better than the current limits. To carry out a search for $\mu^-{-}e^-$ conversion, two types of detector options are being considered. One is a detector dedicated for COMET Phase-I, and the other is a re-use of the detector used for the background measurements.

The former is based on a cylindrical drift chamber which surrounds a muon stopping target. The detector is placed inside a large superconducting solenoid magnet producing a 1 Tesla magnetic field, similarly to the SINDRUM-II detector. From our studies, COMET Phase-I would carry out a search for $\mu^-{-}e^-$ conversion in aluminum with a single-event sensitivity of $3.1 \times 10^{-15}$, which is a factor 200 times better that the current limit by SINDRUM-II. The measurement can be done with a 8 GeV proton beam of 3.2 kW power over a running time of $10^6$ seconds (12 days). The background of about 0.11 events is expected at this sensitivity with a proton extinction factor of $10^{-9}$. The details are described in Chapter 6.

In addition to the $\mu^-{-}e^-$ conversion search, the special features of the COMET Phase-I detector allows for further possibilities:

- This detector can detect both positive and negative particles, whereas the full COMET detector can detect only negatively charged particles owing to the electron transport system which uses curved solenoids. This allows for a search for the lepton-number-violating process $\mu^- + N \to e^+ + N'$ ($\mu^-{-}e^+$ conversion) concurrently with the $\mu^-{-}e^-$ conversion search. The anticipated experimental sensitivity for $\mu^-{-}e^+$ conversion could be similar to $\mu^-{-}e^-$ conversion, although a detailed estimation has not been performed.
- This detector can have a large geometrical coverage, and thereby a coincidence measurement with a large solid angle is achievable. And also the J-PARC MR can provide a DC proton beam with a duty factor of about 0.3. These facts indicate that a search for $\mu^- + e^- \to e^- + e^-$ conversion in a muonic atom is possible. This is a previously-unmeasured process. With a beam of less than $10^7$ muons/sec in intensity, a measurement of $\mu^- + e^- \to e^- + e^-$ can be carried out by this detector.

### 1.2.3 Towards the Full COMET Experiment (COMET Phase-II)

The addition of the full muon beamline in Phase-II will give the ultimate single-event sensitivity for the COMET experiment of $3 \times 10^{-17}$. The proposed staged approach will produce valuable scientific outcomes at each phase and the physics impact of our CLFV search in COMET Phase-I will be significant.

# Chapter 2

# Physics Motivation

## 2.1 Introduction

The origin of the flavors of elementary particles is a puzzling enigma. Their properties and structure should reflect the nature of the physics beyond the Standard Model (SM). Flavor physics is thereby believed to provide a path to new physics. The flavor-changing neutral current (FCNC) processes are of particular interest since they are expected to include the effect of new physics that are observable in high-precision experiments. Among the FCNC processes, the charged lepton flavor violation (CLFV) processes have recently attracted much attention from both theoretical and experimental points of views. The search for CLFV processes has notable advantages, including the following. (1) CLFV can have **sizable contributions from new physics** and thus can manifest themselves in future experiments. (2) CLFV gives **no sizable contribution in the Standard Model** unlike the FCNC process of the quarks; such contributions give serious background events and limit the sensitivity to new physics.

## 2.2 New Physics and CLFV

Although CLFV has never been observed, LFV among neutrino species has been experimentally confirmed with the discovery of neutrino oscillations [15, 16], and hence lepton flavor conservation is now known to be violated. The phenomenon of oscillation means that neutrinos are massive and hence the SM must be modified so that LFV can occur. Furthermore, there are other reasons which compel us to modify the SM, including the existence of dark matter, and stability of the weak scale against quantum corrections. These indicate that new physics beyond the SM will reveal itself at the TeV scale. This scale is within the scope of the Large Hadron Collider and expected CLFV experiments including COMET and COMET Phase-I.

It is well known that in the minimally extended SM, which includes vanishingly small neutrino masses to account for neutrino oscillations, the predicted rate for CLFV is too small to be observed. For example, the prediction for $\mathrm{Br}(\mu \to e\gamma)$ is given by the graph in Figure 2.1 [17, 18, 19, 20],

$$\mathrm{Br}(\mu \to e\gamma) = \frac{\alpha}{2\pi}\left|\sum_k U_{ek}U_{\mu k}^* \frac{m_{\nu_k}^2}{m_W^2}\right|^2 \simeq \frac{\alpha}{2\pi}\left|U_{e3}U_{\mu 3}^*\frac{\delta m_{\mathrm{atm}}^2}{m_W^2}\right|^2 < 10^{-54}. \tag{2.1}$$

Table 2.1: Present limits of LFV of the muon, tau, pion, kaon and $Z$ boson.

| Reaction | Present limit | Reference |
|---|---|---|
| $\mu^+ \to e^+\gamma$ | $< 1.2 \times 10^{-11}$ | [2] |
| $\mu^+ \to e^+e^+e^-$ | $< 1.0 \times 10^{-12}$ | [3] |
| $\mu^- Ti \to e^- Ti$ | $< 6.1 \times 10^{-13}$ | [4] |
| $\mu^- Au \to e^- Au$ | $< 7 \times 10^{-13}$ | [1] |
| $\mu^+e^- \to \mu^-e^+$ | $< 8.3 \times 10^{-11}$ | [5] |
| $\tau \to e\gamma$ | $< 3.9 \times 10^{-7}$ | [6] |
| $\tau \to \mu\gamma$ | $< 3.1 \times 10^{-7}$ | [7] |
| $\tau \to \mu\mu\mu$ | $< 1.9 \times 10^{-7}$ | [8] |
| $\tau \to eee$ | $< 2.0 \times 10^{-7}$ | [8] |
| $\pi^0 \to \mu e$ | $< 8.6 \times 10^{-9}$ | [9] |
| $K_L^0 \to \mu e$ | $< 4.7 \times 10^{-12}$ | [10] |
| $K^+ \to \pi^+\mu^+e^-$ | $< 2.1 \times 10^{-10}$ | [11] |
| $K_L^0 \to \pi^0\mu^+e^-$ | $< 3.1 \times 10^{-9}$ | [12] |
| $Z^0 \to \mu e$ | $< 1.7 \times 10^{-6}$ | [13] |
| $Z^0 \to \tau e$ | $< 9.8 \times 10^{-6}$ | [13] |
| $Z^0 \to \tau\mu$ | $< 1.2 \times 10^{-5}$ | [14] |

Here $U_{\beta i}$ is the Maki-Nakagawa-Sakata Matrix [21] with $\beta$ denoting a charged lepton flavor eigenstate and $i$ a neutrino mass eigenstate with mass $m_i$, and $m_W$ is the $W$ boson mass, and $\alpha$ is the fine structure constant. Note that the GIM mechanism [22] leads to a prediction dependent on differences in the masses of the neutrinos. For the $\mu \to e\gamma$ process, a similar suppression arises due to gauge symmetry.

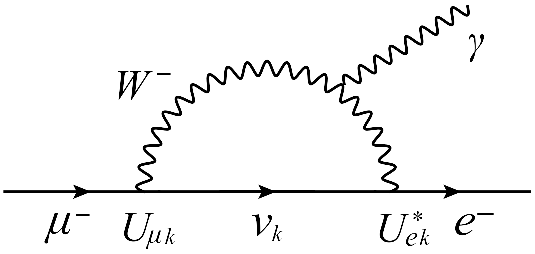

Figure 2.1: One of the diagrams of massive neutrino contributions to a $\mu$ to $e$ transition ($\mu \to e$ "$\gamma$").

Therefore, the discovery of LFV would imply new physics beyond not only the SM but also beyond "neutrino oscillations". In fact, all new physics or interactions beyond the Standard Model predict LFV at some level. Examples of such new physics models include supersymmetric (SUSY) models, extra dimension models, little Higgs models, models with new gauge $Z'$ bosons, models with new heavy leptons, lepto-quark models, etc.. Each gives a prediction for flavor changing neutral currents (FCNC), including CLFV.

## 2.3 CLFV at the LHC Era

At the time of writing this LoI, no new physics phenomena has been found at the LHC. Therefore, the search for CLFV is crucial to find any clues of new physics beyond the SM. There are many other models to account for neutrino LFV (lepton mixing and neutrino masses), the existence of dark matter, the stability of the electroweak scale and so on. All of them predict a new particle at the TeV scale which will be found LHC. Each model has its prediction for Br($\mu \to e\gamma$) and Br($\mu^- + N \to e^- + N$). These are parametrized in the effective operator as

$$\mathcal{L} = \frac{a_{\mu e}^2 m_\mu}{\Lambda} \bar{e}\sigma^{\mu\nu} F_{\mu\nu}\mu + \frac{b_{\mu e}^2}{\Lambda} \bar{e}\mu\bar{q}q. \tag{2.2}$$

Here $\Lambda$ indicates a typical new physics scale and $a_{\mu e}^2$ and $b_{\mu e}^2$ stand for couplings and/or loop factors. The current limits of CLFV [2, 3, 4] give a stringent limit on these effective scales as $\Lambda/a_{\mu e}, \Lambda/b_{\mu e} > 10^3$ TeV. It means, for example, if these operators are loop suppressed, the scale explored by new CLFV experiments is the TeV range.

In general, the relation between $a_{\mu e}$ and $b_{\mu e}$ is model dependent. For example in a SUSY model they are both loop suppressed and are related with each other tightly while in a Little Higgs model, they are both loop suppressed but are not related so much. Therefore the relation between $\mu \to e\gamma$ and $\mu^-{-}e^-$ conversion shows a characteristic feature for each model. It is expected that the LHC will find evidence for new physics. It is, however very difficult to discriminate a true model from other candidates. It is, therefore, essential to determine the relation between $a_{\mu e}$ and $b_{\mu e}$.

This demonstrates that the $\mu^-{-}e^-$ conversion search has outstanding physics motivation, even in the LHC era and after the MEG experiment.

## 2.4 $\mu^-{-}e^-$ Conversion

### 2.4.1 What is a $\mu^-{-}e^-$ conversion process ?

One of the most prominent muon LFV processes is coherent neutrinoless conversion of muons to electrons ($\mu^-{-}e^-$ conversion). When a negative muon is stopped by some material, it is trapped by an atom, and a muonic atom is formed. After it cascades down energy levels in the muonic atom, the muon is bound in its $1s$ ground state. The fate of the muon is then to either decay in orbit ($\mu^- \to e^-\nu_\mu\overline{\nu}_e$) or be captured by a nucleus of mass number $A$ and atomic number $Z$, namely, $\mu^- + N(A,Z) \to \nu_\mu + N(A, Z-1)$. However, in the context of physics beyond the Standard Model, the exotic process of neutrinoless muon capture, such as

$$\mu^- + N(A,Z) \to e^- + N(A,Z), \tag{2.3}$$

is also expected. This process is called $\mu^-{-}e^-$ conversion in a muonic atom. This process violates the conservation of lepton flavor numbers, $L_e$ and $L_\mu$, by one unit, but the total lepton number, $L$, is conserved. The final state of the nucleus $(A, Z)$ could be either the ground state or one of the excited states. In general, the transition to the ground state, which is called coherent capture, is dominant. The rate of the coherent capture over non-coherent capture is enhanced by a factor approximately equal to the number of nucleons in the nucleus, since all of the nucleons participate in the process.

### 2.4.2 Signal and background events

The event signature of coherent $\mu^-{-}e^-$ conversion in a muonic atom is a mono-energetic single electron emitted from the conversion with an energy of $E_{\mu e} \sim m_\mu - B_\mu$, where $m_\mu$ is the muon mass and $B_\mu$ is the binding energy of the $1s$ muonic atom.

From an experimental point of view, $\mu^-{-}e^-$ conversion is a very attractive process. Firstly, the $e^-$ energy of about 105 MeV is far above the end-point energy of the muon decay spectrum ($\sim$ 52.8 MeV). Secondly, since the event signature is a mono-energetic electron, no coincidence measurement is required. The search for this process has the potential to improve sensitivity by using a high muon rate without suffering from accidental background events, which would be serious for other processes, such as $\mu^+ \to e^+\gamma$ and $\mu^+ \to e^+e^+e^-$ decays.

The electron is emitted with an energy $E_e \approx m_\mu$, which coincides with the endpoint of muon decay in orbit (DIO), which is the only relevant intrinsic physics background event. Since the energy distribution of DIO falls steeply above $m_\mu/2$, the experimental setup can have a large signal acceptance and the detectors can still be protected against the vast majority of decay and capture background events. Energy distributions for DIO electrons have been calculated for a number of muonic atoms [23, 24] and energy resolutions of the order of 0.1% are sufficient to keep this background below $10^{-18}$.

There are several other potential sources of electron background events in the energy region around 100 MeV, involving either beam particles or cosmic rays. Beam-related background events may originate from muons, pions or electrons in the beam. Apart from DIO, muons may produce background events by muon decay in flight or radiative muon capture (RMC). Pions may produce background events by radiative pion capture (RPC). Gamma rays from RMC and RPC produce electrons mostly through $e^+e^-$ pair production inside the target.

There are three methods to suppress the beam-related background events:

- Beam pulsing
  Since muonic atoms have lifetimes of the order of 1 $\mu$s, a pulsed beam with buckets that are short compared with this lifetime would allow the removal of prompt background events by performing measurements in a delayed time window. As will be discussed below there are stringent requirements on beam extinction during the measuring interval.
- Beam purity
  The lifetime of the pion (26 ns) is much shorter than the lifetime of muon (2200 ns). Thus, if the beam momentum is low enough, most of beam pions will decay away as they transport through a muon beamline. If the beam momentum is less than 70 MeV/$c$, the level of pion contamination will be decreased by an order of magnitude for each 10 m.
- Beam momentum
  The in-flight decay of beam muons produces 100 MeV/$c$ electrons if the beam momentum is larger than 70 MeV/$c$. Beam electrons would be also a source of 100 MeV/$c$ electron background. Thus, if the beam momentum is restricted to be lower than 70 MeV/$c$, these backgrounds can be suppressed.

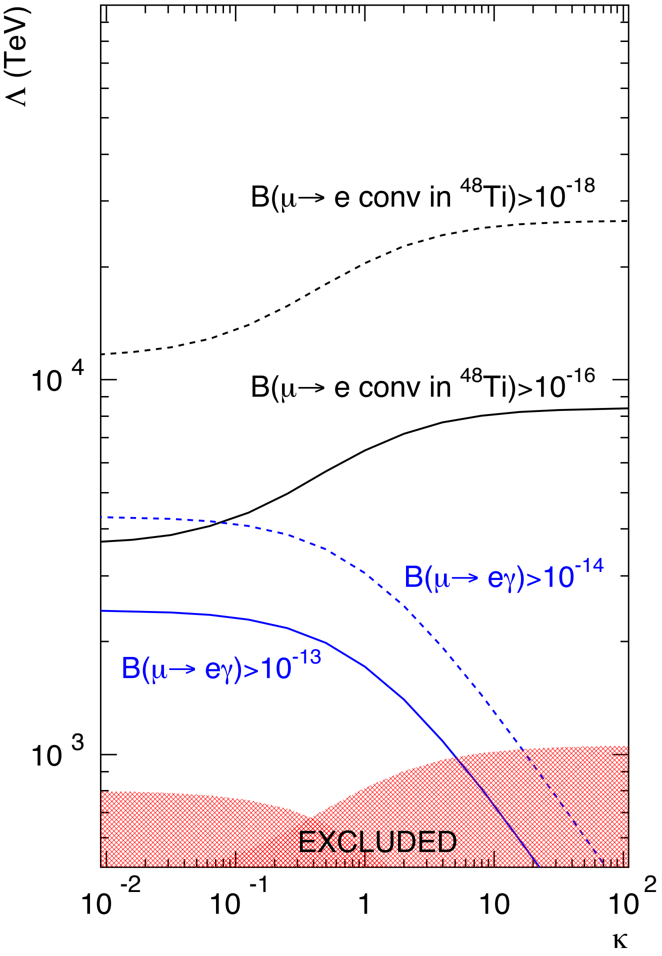

Figure 2.2: Relation between $\mu^+ \rightarrow e^+\gamma$ and $\mu^-{-}e^-$ conversion. A parameter of $\kappa$ interpolates between the photonics and the non-photonic contributions. By using the parameters in Eq.(2.2), $a_{\mu e} = 1/(1+\kappa)$ and $b_{\mu e} = \kappa/(1+\kappa)$ are given.

### 2.4.3 $\mu^-{-}e^-$ conversion vs. $\mu^+ \rightarrow e^+\gamma$

There are considered to be two possible contributions in the $\mu^-{-}e^-$ transition diagrams. One is a photonic contribution, and the other is a non-photonic contribution. For the photonic contribution, there is a definite relation between the $\mu^-{-}e^-$ conversion process and the $\mu^+ \rightarrow e^+\gamma$ decay. Suppose the photonic contribution is dominant, the branching ratio of the $\mu^-{-}e^-$ conversion process is expected be smaller than that of $\mu^+ \rightarrow e^+\gamma$ decay by a factor of a few hundred due to electromagnetic interaction of a virtual photon. This implies that the search for $\mu^-{-}e^-$ conversion at the level of $10^{-16}$ is comparable to that for $\mu^+ \rightarrow e^+\gamma$ at the level of $10^{-14}$.

If the non-photonic contribution dominates, the $\mu^+ \rightarrow e^+\gamma$ decay would be small whereas the $\mu^-{-}e^-$ conversion could be sufficiently large to be observed. It is worth noting the following. If a $\mu^+ \rightarrow e^+\gamma$ signal is found, the $\mu^-{-}e^-$ conversion signal should also be found. A ratio of the branching ratios between $\mu^+ \rightarrow e^+\gamma$ and $\mu^-{-}e^-$ carries vital information on the intrinsic physics process. If no $\mu^+ \rightarrow e^+\gamma$ signal is found, there will still be an opportunity to find a $\mu^-{-}e^-$ conversion signal because of the potential existence of non-photonic contributions. Figure 2.2 shows the relation between the branching ratios of $\mu^+ \rightarrow e^+\gamma$ and $\mu^-{-}e^-$ conversion in terms of as a function of a ratio of the photonic and non-photonic contributions.

### 2.4.4 Why is $\mu^-{-}e^-$ conversion the next step ?

Considering its marked importance to physics, it is highly desirable to consider a next-generation experiment to search for LFV. There are three processes to be considered; namely, $\mu^+ \to e^+\gamma$, $\mu^+ \to e^+e^+e^-$, and $\mu^-{-}e^-$ conversion.

The three processes have different experimental issues that need to be solved to realize improved experimental sensitivities. They are summarized in Table 2.2. The processes of $\mu^+ \to e^+\gamma$ and $\mu^+ \to e^+e^+e^-$ are detector-limited. To consider and go beyond the present sensitivities, the resolutions of detection have to be improved, which is, in general, very hard. In particular, improving the photon energy resolution is difficult. On the other hand, for $\mu^-{-}e^-$ conversion, there are no accidental background events, and an experiment with higher rates can be performed. If a new muon source with a higher beam intensity and better beam quality for suppressing beam-associated background events can be constructed, measurements of higher sensitivity can be performed.

Table 2.2: LFV processes and issues

| Process | Major backgrounds | Beam | Sensitivity Issues |
|---|---|---|---|
| $\mu^+ \to e^+\gamma$ | accidental | DC beam | detector resolution |
| $\mu^+ \to e^+e^+e^-$ | accidental | DC beam | detector resolution |
| $\mu^-{-}e^-$ conversion | beam-associated | pulsed beam | beam qualities |

Furthermore, it is known that in comparison with $\mu^+ \to e^+\gamma$, there are more physical processes that $\mu^-{-}e^-$ conversion and $\mu^+ \to e^+e^+e^-$ could contribute to. Namely, in SUSY models, photon-mediated diagrams can contribute to all the three processes, but the Higgs-mediated diagrams can contribute to only $\mu^-{-}e^-$ conversion and $\mu^+ \to e^+e^+e^-$. In summary, with all of the above considerations, a $\mu^-{-}e^-$ conversion experiment would be the natural next step in the search for lepton flavour violation.

### 2.4.5 Present experimental status of $\mu^-{-}e^-$ conversion

Table 2.3 summarizes the history of searches for $\mu^-{-}e^-$ conversion. From Table 2.3, it is seen that over about 30 years the experimental upper limits has been improved by 5 orders of magnitude. In the following, the past and future experiments of searching for $\mu^-{-}e^-$ conversion will be described.

#### 2.4.5.1 SINDRUM-II

The latest search for $\mu^-{-}e^-$ conversion was performed by the SINDRUM-II collaboration at PSI. Figure 2.3 shows their results. The main spectrum, taken at 53 MeV/$c$, shows the steeply falling distribution expected from muon DIO. Two events were found at higher momenta, but just outside the region of interest. The agreement between measured and simulated positron distributions from $\mu^+$ decay means that confidence can be high in the accuracy of the momentum calibration. At present there are no hints concerning the nature of the two high-momentum events: they might have been induced by cosmic rays or RPC, for example. They set the current upper limit on $B(\mu^- + \mathrm{Au} \to e^- + \mathrm{Au}) < 7 \times 10^{-13}$ [1].

Table 2.3: Past experiments on $\mu^- - e^-$ conversion. (* reported only in conference proceedings.)

| Process | upper limit | place | year | reference |
|---|---|---|---|---|
| $\mu^- + Cu \to e^- + Cu$ | $< 1.6 \times 10^{-8}$ | SREL | 1972 | [25] |
| $\mu^- + {}^{32}S \to e^- + {}^{32}S$ | $< 7 \times 10^{-11}$ | SIN | 1982 | [26] |
| $\mu^- + Ti \to e^- + Ti$ | $< 1.6 \times 10^{-11}$ | TRIUMF | 1985 | [27] |
| $\mu^- + Ti \to e^- + Ti$ | $< 4.6 \times 10^{-12}$ | TRIUMF | 1988 | [28] |
| $\mu^- + Pb \to e^- + Pb$ | $< 4.9 \times 10^{-10}$ | TRIUMF | 1988 | [28] |
| $\mu^- + Ti \to e^- + Ti$ | $< 4.3 \times 10^{-12}$ | PSI | 1993 | [29] |
| $\mu^- + Pb \to e^- + Pb$ | $< 4.6 \times 10^{-11}$ | PSI | 1996 | [30] |
| $\mu^- + Ti \to e^- + Ti$ | $< 6.1 \times 10^{-13}$ | PSI | 1998* | [4] |
| $\mu^- + Au \to e^- + Au$ | $< 7 \times 10^{-13}$ | PSI | 2006 | [1] |

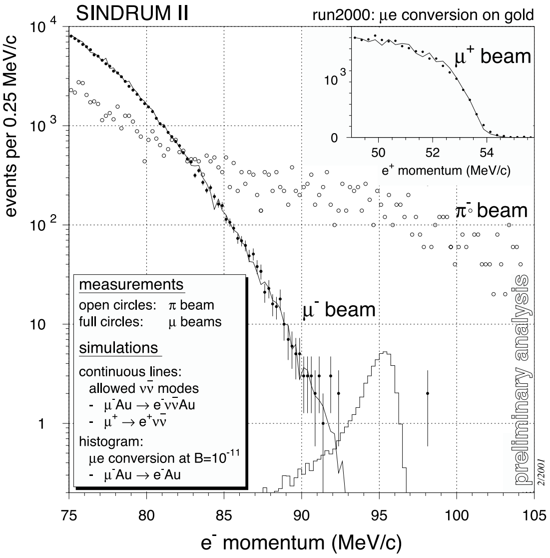

Figure 2.3: Recent results by SINDRUM-II. Momentum distributions for three different beam momenta and polarities: (i) 53 MeV/$c$ negative, optimized for $\mu^-$ stops, (ii) 63 MeV/$c$ negative, optimized for $\pi^-$ stops, and (iii) 48 MeV/$c$ positive, optimized for $\mu^+$ stops. The 63 MeV/$c$ data were scaled to the different measuring times. The $\mu^+$ data were taken using a reduced spectrometer field.

#### 2.4.5.2 MECO

There was an experimental proposal at BNL, the MECO experiment [31], aiming to search with a sensitivity of $10^{-16}$. This project was planned to combat beam-related background events with the help of a pulsed 8 GeV/$c$ proton beam. Figure 2.4 shows the proposed layout. Pions are produced by 8 GeV/$c$ protons crossing a 16 cm long tungsten target, and muons from the decays of the pions are collected efficiently with the help of a graded magnetic field. Negatively charged particles with 60–120 MeV/$c$ momenta are transported by a curved solenoid to the experimental target. In the spectrometer magnet, a graded field is also applied. A major challenge is the requirement for proton extinction in between the proton bursts. In order to maintain the pion stop rate in the 'silent' interval, a beam extinction factor better than $10^{-8}$–$10^{-9}$ is required. Unfortunately, the MECO experiment was canceled in 2005, owing to the NSF funding problems.

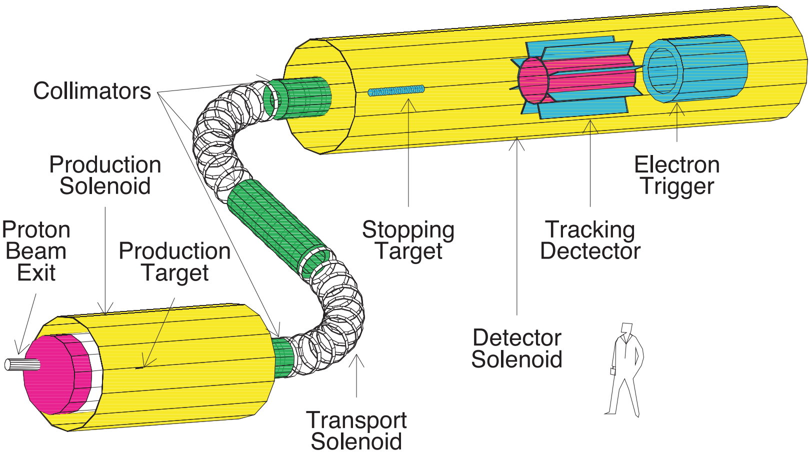

Figure 2.4: Setup of the MECO experiment.

### 2.4.5.3 Mu2e

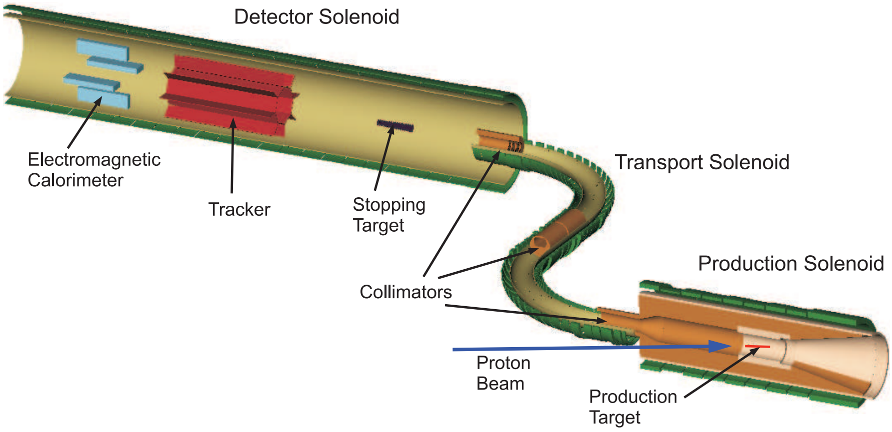

Figure 2.5: A schematic layout of the Mu2e experiment.

However, the revival of the MECO experiment has been actively made at the Fermi National Laboratory (Fermilab), the “Mu2e experiment” (see Fig. 2.5). The muon beam line and detector for the Mu2e experiment are almost the same as those of the MECO experiment. The aimed experimental sensitivity is also the same. The experimental proposal was stage-one approved at Fermilab fall, 2008 [32]. The Mu2e experiment would strongly compete with the COMET experiment. The Mu2e experiment will use the Fermilab proton source, and the desired proton beam structure from their 8 GeV Booster can be made by reusing the 8 GeV Debuncher and Accumulator storage rings, which are both housed in the anti-proton beam enclosure.

## 2.5 Other Muon CLFV Physics Processes

The other muon CLFV processes that can be potentially searched for at COMET Phase-I are presented. They are $\mu^-{-}e^+$ conversion and $\mu^- + e^- \to e^- + e^-$ in a muonic atom.

### 2.5.1 $\mu^-{-}e^+$ conversion process

The other neutrinoless muon-conversion process is a charge-changing reaction, such as

$$\mu^- + N(A,Z) \to e^+ + N(A,Z-2)^*, \tag{2.4}$$

which violates the conservation of total lepton number (LFV) as well as the lepton flavor numbers, $L_e$ and $L_\mu$. This process is closely related to neutrinoless double $\beta-$decay ($\beta\beta_{0\nu}$), since both processes require a mechanism involving two nucleons. The final state of the nucleus $N(A,Z-2)^*$ could be either the ground state ($gs$) or an excited state ($ex$). Since the final nucleus is not the same as the initial nucleus, no coherent enhancement is expected, even for the transition to the ground state. The branching ratio of $\mu^-{-}e^+$ conversion is defined by

$$B(\mu^- N(A,Z) \to e^+ N(A,Z-2)^*) \equiv \frac{\Gamma(\mu^- N(A,Z) \to e^+ N(A,Z-2)^*)}{\Gamma(\mu^- N(A,Z) \to \text{capture})}. \tag{2.5}$$

Various theoretical models predict experimentally accessible rates. One is the minimum supersymmetric model (MSSM) with R-parity violation, which allows a branching ratio for $\mu^-{-}e^+$ conversion of about $10^{-12}$, since the relevant $\lambda$ and $\lambda'$ parameters are not constrained [33]. Left-right symmetric models with a low-mass $W_R$ also predict a $\mu^-{-}e^+$ conversion branching ratio of $10^{-14}$.

#### 2.5.1.1 Event signature and backgrounds

The energy of the positron from $\mu^-{-}e^+$ conversion is given by

$$\begin{aligned} E_{\mu e^+} &= m_\mu - B_\mu - E_{rec} - \Delta_{Z-2} \\ &\approx m_\mu - B_\mu - \Delta_{Z-2}, \end{aligned} \tag{2.6}$$

where $\Delta_{Z-2}$ is the difference in the nuclear binding energy between the $(A,Z)$ and $(A,Z-2)$ nuclei, with the excitation energy in the final nucleus taken into account. Usually, it is assumed that a large fraction of the final nucleus could be in the giant dipole resonance state, which has a mean energy of 20 MeV and a width of 20 MeV. Therefore, the $e^+$ from $\mu^-{-}e^+$ conversion would have a broad momentum distribution corresponding to the width of giant dipole resonance excitation.

The principal background is radiative muon capture (RMC) or radiative pion capture (RPC), followed by asymmetric $e^+e^-$ conversion of the photon. For some nuclei, the endpoint of the RMC background can be selected to be well separated from the signal. The background from RPC must be reduced by the rejection of pions in the beam.

Table 2.4: Historical progress and summary of $\mu^-{-}e^+$ conversion in various nuclei. *gs* and *ex* respectively denote the transitions to the ground state and excited states (mostly giant dipole-resonance states), respectively.

| Process | 90% C.L. upper limit | place | year | reference |
|---|---|---|---|---|
| $\mu^- + Cu \to e^+ + Co$ | $2.6 \times 10^{-8}$ | SREL | 1972 | [25] |
| $\mu^- + S \to e^+ + Si$ | $9 \times 10^{-10}$ | SIN | 1982 | [26] |
| $\mu^- + Ti \to e^+ + Ca(gs)$ | $9 \times 10^{-12}$ | TRIUMF | 1988 | [28] |
| $\mu^- + Ti \to e^+ + Ca(ex)$ | $1.7 \times 10^{-10}$ | TRIUMF | 1988 | [28] |
| $\mu^- + Ti \to e^+ + Ca(gs)$ | $4.3 \times 10^{-12}$ | PSI | 1993 | [29] |
| $\mu^- + Ti \to e^+ + Ca(ex)$ | $8.9 \times 10^{-11}$ | PSI | 1993 | [29] |
| $\mu^- + Ti \to e^+ + Ca(gs)$ | $1.7 \times 10^{-12}$ | PSI | 1998 | [34] |
| $\mu^- + Ti \to e^+ + Ca(ex)$ | $3.6 \times 10^{-11}$ | PSI | 1998 | [34] |

#### 2.5.1.2 Experimental status of $\mu^-{-}e^+$ conversion

The SINDRUM-II Collaboration at PSI has reported a search for the charge-changing process $\mu^- + Ti \to e^+ + Ca$ in muonic atoms [34]. It was carried out simultaneously with a measurement of $\mu^- + Ti \to e^- + Ti$. The results are given separately for the transition to the ground state and that to the giant dipole resonance. They are summarized in Table 2.4, together with the previous results.

### 2.5.2 $\mu^- + e^- \to e^- + e^-$ conversion process

The other CLFV process in a muonic atom is

$$\mu^- + e^- \to e^- + e^-, \tag{2.7}$$

where $e^-$ in the initial state is an atomic electron in a muonic atom. This process violates the conservation of the lepton flavor numbers, $L_e$ and $L_\mu$. This process is closely related to $\mu^+ \to e^+e^+e^-$ decay [35]. The advantage of $\mu^- + e^- \to e^- + e^-$ over $\mu^+ \to e^+e^+e^-$ is that the final state has clear kinematics of two body decays. The disadvantage is small overlap of the wave functions of $\mu^-$ and $e^-$ in the initial state. Since the wave function of the 1$s$ atomic electrons in a muonic atom are determined by the atomic number of the nucleus $Z$, when a heavy target material is used, the rate will be increased by $Z^3$. There have been no experimental limits on this process and so any measurement would have significant impact.

# Chapter 3

# Proton Beam

This chapter describes the proton beam used to produce the COMET muon beam. The J-PARC main ring (MR) is used to supply a pulsed 8 GeV proton beam, which is slow extracted, maintaining its bunch structure, into the J-PARC Nuclear and Particle Experimental Hall (NP Hall). The pulsed proton beam then hits the pion production target located inside the pion capture solenoid magnet. The produced pions decay to muons as they are transported from the pion production target to the muon stopping target. These muons are momentum selected by the curved solenoid transport channel as described in Chapter 4. Phase-I of the COMET experiment requires the same beam structure as proposed in the COMET experiment.

## 3.1 Requirements for the proton beam

The J-PARC MR will deliver a proton beam, as the design goal, with an intensity of $3.3\times10^{14}$ protons per cycle and a cycle time of about 0.3 Hz. Protons from the J-PARC MR are extracted either to the NP Hall by slow extraction, or to the neutrino experimental hall (T2K) by fast extraction. When operated in slow extraction mode, the average beam current and duty factor are 15 $\mu$A and 0.2 respectively.

Since COMET Phase-I requires the intensity of muons on the stopping target to be as high as tolerable for the detector system, the intensity of the proton beam needs to be high enough in order to provide an intense flux of pions.

### 3.1.1 Proton energy

The number of pions (and therefore their daughter muons) produced by a proton beam is proportional to the proton beam power, which is given by the product of the beam energy and beam current. This is due to the fact that the pion cross-section increases linearly with proton beam energy.

The required beam power in Phase-I is approximately 1 to 2 orders of magnitude lower than that for the full COMET experiment. The reasons for the relatively low proton beam energy, i.e. 8 GeV, are twofold. One is to suppress production of anti-protons, and the other is to ease the requirements of the beam extinction system if needed, where a lower beam energy is easier to deflect. The cross section of anti-proton production, $p + p \to p + p + p + \bar{p}$ whose threshold is at 5.6 GeV, rapidly increases above a proton beam energy of 10 GeV as shown in Figure 3.1. Thus a proton beam energy of 8 GeV

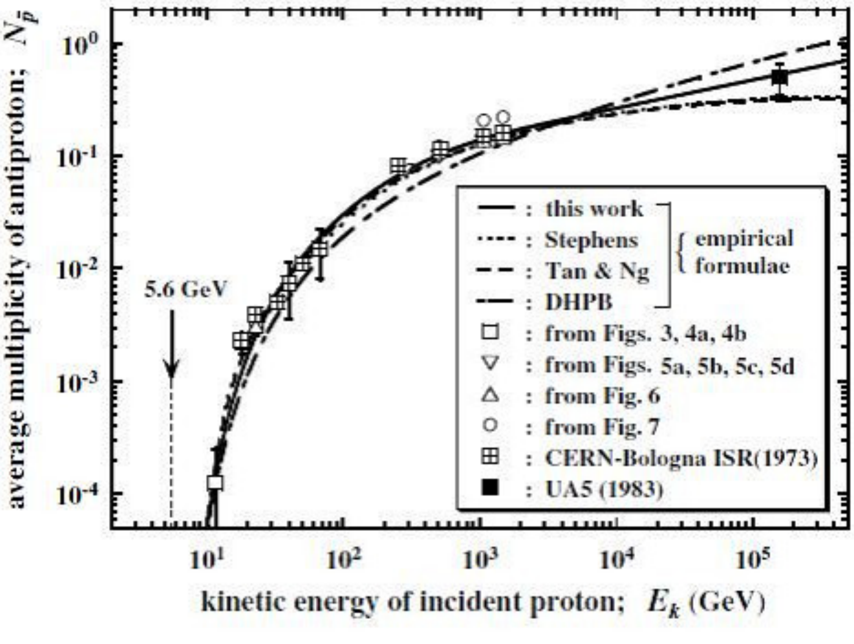

Figure 3.1: Average multiplicity of anti-proton production as a function of the incident proton energy [36].

is used in the current design. At this energy, even if anti-protons are produced, most of them can be eliminated by inserting a stopping foil in the muon transport line. The foil separating the vacuum between the COMET experimental area and the primary beam line can be used for this purpose.

### 3.1.2 Proton beam power

The required proton beam power is 8 GeV × (0.1–1) $\mu$A ((0.63–6.3) $\times$ $10^{12}$ protons/s), which will provide enough muons at COMET Phase-I to allow the beam properties to be studied and the physics goals to be achieved. We start at lower intensities, which are also suitable for performing the accelerator studies that are needed to realize 8 GeV beam extraction from the MR. If the beam power could be upgraded by increasing the repetition cycle of the accelerator, that is ideal for COMET Phase-I, whose sensitivity reach will be limited by the detector hit rate. For example, reducing the acceleration and extraction cycle time by a factor of two will provide twice the beam power without modifying the proton time structure and detector.

### 3.1.3 Proton beam time structure

There are two main purposes to COMET Phase-I; to study the properties of the beam and to conduct a $\mu - e$ conversion search. For the former purpose, a normal slow-extraction beam is best for reducing the instantaneous detector hit rate. For the latter, as in the case of $\mu - e$ conversion search using the full COMET experiment, the proton beam needs to be pulsed with a time separation of about 1 $\mu$s, which corresponds to the lifetime of a muon in a muonic atom. The signal electrons are emitted from the stopping target and enter the detector during the interval between proton pulses. The beam-related background come within a few hundred ns after the proton pulse since these are mostly prompt processes. This timing information is very important for distinguishing signal events from background events. It is also very important to reduce the number of residual protons between pulses as these produce beam-related background in the signal timing window. For COMET Phase-I to achieve its expected sensitivity, the relative number of residual protons between pulses needs to be as small as the requirement for the full COMET experiment, namely $10^9$ times smaller than the number of protons in the main pulse, because of the shorter length of the muon transport line, which leads to a larger survival rate for the pions.

Table 3.1 summarizes the required parameters of the pulsed proton beam for COMET Phase-I $\mu - e$ conversion search. They are almost same as the COMET final configuration except the beam power. Figure 3.2 shows a typical time structure for the pulsed proton beam suitable for the COMET experiment.

Table 3.1: Pulsed proton beam for the COMET experiment.

| | |
|---|---|
| Beam Power | 8 kW |
| Energy | 8 GeV |
| Average Current | 1 $\mu$A |
| Beam Emittance | $10\,\pi$ mm·mrad |
| Protons per Bunch | $< 10^{10}$ |
| Extinction | $10^{-9}$ |
| Bunch Separation | 1∼2 $\mu$s |
| Bunch Length | 100 ns |

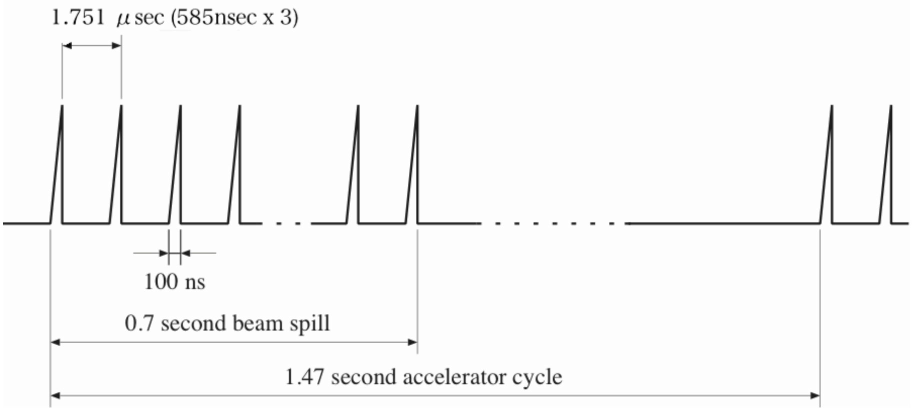

Figure 3.2: Bunched proton beam in a slow extraction mode.

## 3.2 Acceleration

Proton beam acceleration for COMET Phase-I is, in principle, identical to that for the final COMET configuration in all aspects but the beam power. As described in the COMET proposal and CDR [37], COMET requires a special operation mode of the J-PARC MR in order to obtain the required beam structure. The time between two consecutive bunches should be as long as the muon life time when bound by a nucleus, i.e. 1–2 $\mu$s, and the bunch width should be small ($\sim$100 ns) compared to this. In addition to this the proton beam has to be transported to the pion production target whilst keeping its pulse structure. This can be realized using the bunched slow extraction technique. The requirements on the time structure are satisfied by operating the MR by filling only three out of nine buckets in the case when the ring is operated at a harmonic number of nine. The three filled buckets are distributed along the ring in such a way that two empty buckets exist between two filled buckets. Since the time difference between two consecutive buckets is 585 ns, as determined by the acceleration RF frequency, the bunch-bunch spacing will then be 1.751 $\mu$s. This satisfies the COMET proton pulse separation requirement.

We now discuss in further detail the J-PARC accelerator chain, which consists of the Linac, a Rapid-Cycling Synchrotron (RCS) and the Main Ring (MR).

### 3.2.1 LINAC operation

Operation of the proton Linac will be almost the same as that in normal operation mode [38]. The proton beam bunch structure needed to fill the RCS is formed by a high-frequency chopper cavity and scraper installed in the Linac system. The chopper has a very fast rise time of 10 ns in order to form a gap in the bunch structure to allow the RCS to be filled without producing huge losses.

### 3.2.2 RCS operation

The RCS accepts the beam from the Linac, accelerates it to 3 GeV, and then passes it to the MR for further acceleration. The injection energy of the RCS is currently set to be 181 MeV and will be upgraded to 400 MeV in the future. Four sets of accelerations with two bunches (with a harmonic number of 2) are performed in the RCS for each MR acceleration cycle. Those four pairs of bunches are passed to the MR successively after acceleration at the RCS. For the COMET experiment and COMET Phase-I physics, the MR is operated with empty buckets interspersed between the buckets containing protons (filled buckets) to enable the necessary proton beam time structure as described in the following. This MR beam bunch configuration is realized by configuring the order of filled and empty buckets in the four RCS acceleration cycles. This RCS bunch configuration is possible by changing the chopping time structure in the Linac. One drawback of this scheme is the possible leakage of particles from the filled buckets to the empty buckets during an RCS acceleration cycle, which is caused by the different intermediate-bunch structure produced by the Linac chopper. A systematic study of this leakage effect on the proton beam extinction is being carried out. An innovative method that has been proposed to remove this leakage at the stage of beam injection to the MR will be studied extensively as part of the accelerator development programme for COMET.

### 3.2.3 Main ring operation

The operation scheme of the MR for COMET and COMET Phase-I physics is different from the normal scheme, especially the pulse structure. As already mentioned above,

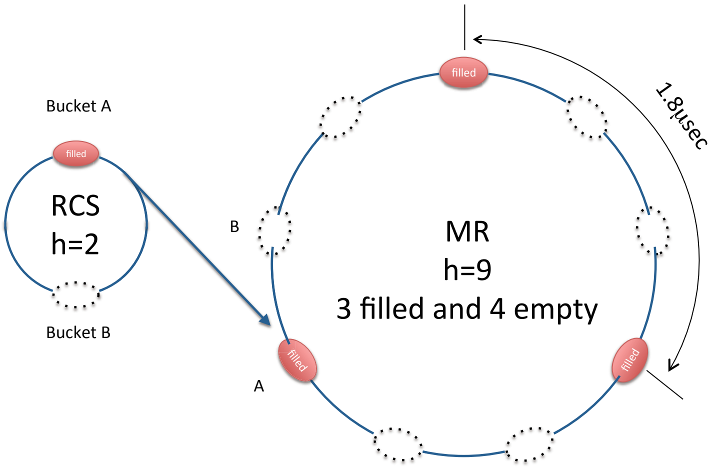

Figure 3.3: COMET beam acceleration bunch configuration.

the COMET beam needs to be pulsed with a pulse separation of 1–2 $\mu$s and pulse width ∼100 ns. This will be realized by filling every third bucket, which gives a total of three out of nine buckets filled in the MR. The scheme is illustrated in Figure 3.3.

#### 3.2.3.1 Injection from the RCS to the MR

Once the proton beam is accelerated to 3 GeV, it is injected to the MR, as is the case for normal operations. A single injection transfers two beam buckets from the RCS to the MR, and this is repeated four times in one MR cycle. The bunch configuration of the RCS needs to be arranged as shown in Table 3.2 to realize the MR bunch configuration, as shown in Figure 3.3. A series of injection kicker magnets kicks the beam bunches to bring the beam on to the MR accelerator orbit. The kickers are excited only once when the beam reaches the end of the transfer line in normal operation mode, while for the COMET beam they are excited again with its phase delayed by half a cycle after the two bunches that have been injected have made one turn in the MR (Figure 3.4). This enables us to sweep away efficiently the particles that remain in the empty buckets because of the inefficiency of the LINAC chopper. A preliminary test of this new injection scheme was conducted in 2010 and has proved to improve the extinction significantly.

Table 3.2: RCS bunch configuration for the COMET acceleration

| Injection | Bucket A | Bucket B |
|---|---|---|
| 1st | filled | empty |
| 2nd | empty | filled |
| 3rd | empty | empty |
| 4th | filled | empty |

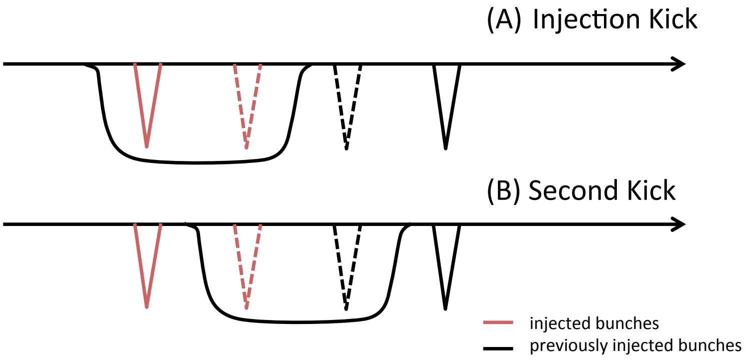

Figure 3.4: Kicker magnets excitation timing after the injected beam bunches make a single turn in the MR.

#### 3.2.3.2 Beam emittance at 8 GeV

The initial emittance of the proton beam before injection is limited by optimizing the collimator in the injection line from the RCS to the MR. The collimator consists of a series of slits and capture jaws which prevent the scraped beam from being transferred into the MR. In normal operation mode the collimator is set to limit the beam emittance to be less than $54\,\pi$ mm·mrad. There are also collimators in the MR itself. These are mainly used to remove the beam halo, which would possibly produce beam loss during further acceleration and extraction, rather than to control the emittance.

The acceptance of the MR slow extraction line and hadron transport line is limited to $25\,\pi$ mm·mrad. The beam emittance is smaller than this in normal operating conditions because of adiabatic damping. However, in accelerator operations for COMET and COMET Phase-I the proton beam is only accelerated up to 8 GeV and therefore the damping effect is smaller than for a 30 GeV beam. This results in the 8 GeV beam having a larger emittance than the acceptance of the slow extraction and hadron transport lines.

We intend to suppress this large beam emittance for the COMET and COMET Phase-I experiments. The J-PARC MR accelerator group is planning to operate a new “dynamic collimator” system [39]. This was originally designed to further reduce beam loss due to emittance growth during early stages of beam acceleration. The system is designed to be applied while the beam is accelerated up to 9 GeV, which is suitable for the COMET beam of 8 GeV. The system is composed of three components configured in the MR as shown in Figure 3.5; a thin target, and a first and second “catcher” made of thick blocks. During acceleration, horizontal and vertical bump orbits are made to optimize the collimation at the catchers as well as scraping at the target. The injection bump magnets and the steering magnets are utilized for COD correction. The thickness of the target and the catchers is optimized by considering the effective collimation from 3 to 9 GeV. The anticipated emittance of the beam is $20.9\,\pi$ mm·mrad at 9 GeV according to simulation studies, which is sufficiently small compared to the acceptance of the MR slow extraction line and hadron transport line.

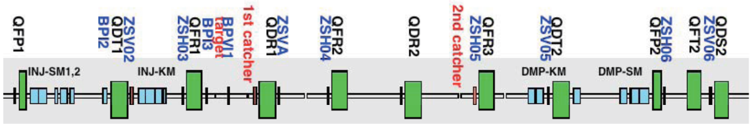

Figure 3.5: Layout of the dynamic collimator system.

#### 3.2.3.3 Extraction

The beam in the MR needs to be extracted and delivered to the pion production target whilst maintaining the pulse structure of the beam. The hardware components used to perform this task for COMET are the same as those used in normal extraction of the 30 GeV beam from the MR.

What is different in the COMET case is that all extraction parameters have to be adjusted and optimized for 8 GeV operation. In addition to this, the RF voltage needs to be kept at a certain value in order to maintain the pulse structure during extraction. In normal slow extraction of the protons from the MR, the RF cavity voltage is usually switched off in order to yield a flat time structure of the proton beam. However, for the COMET experiments, the RF cavity voltage is not switched off in order that the proton pulse structure is maintained when pions are produced at the target. This is referred to as the bunched slow extraction method. It will probably be necessary to reduce the voltage in order to minimize the heat load in the cavities. This needs to be optimized. It is also necessary to modify the feed-back time constant for slow extraction. The COMET beam has a time structure with a frequency of about 1 MHz and this needs to be taken into account in spill control. COMET beam extraction is simulated by using a simple particle tracking method. In Figure 3.6, particle phase space distributions are shown after extraction at the electro-static septum (ESS) magnet. The sharp edges in the $x - x'$ and $x - y$ distributions are due to separation at the ESS. It can be seen in the right-bottom figure that the longitudinal distribution of the particles is less than 20 m. This corresponds to a bunch width of less than 70 ns, which satisfies the COMET beam requirement.

## 3.3 Beam transport

The proton beam transport line is used to take the 8 GeV beam extracted from the MR and deliver it to the pion production target. In spite of the different extraction method to be employed in COMET, the beam transport scheme is the same for COMET and the other experiments at the NP Hall which use the normal slow extracted beam. A conceptual design for the beam transport line is shown in the COMET CDR [37]. Further optimization is necessary before construction, taking into account the availability of hardware, beam separation from the A-line, and the beam switching scheme between the high-momentum primary line which shares the upstream beam line and the COMET beam line.

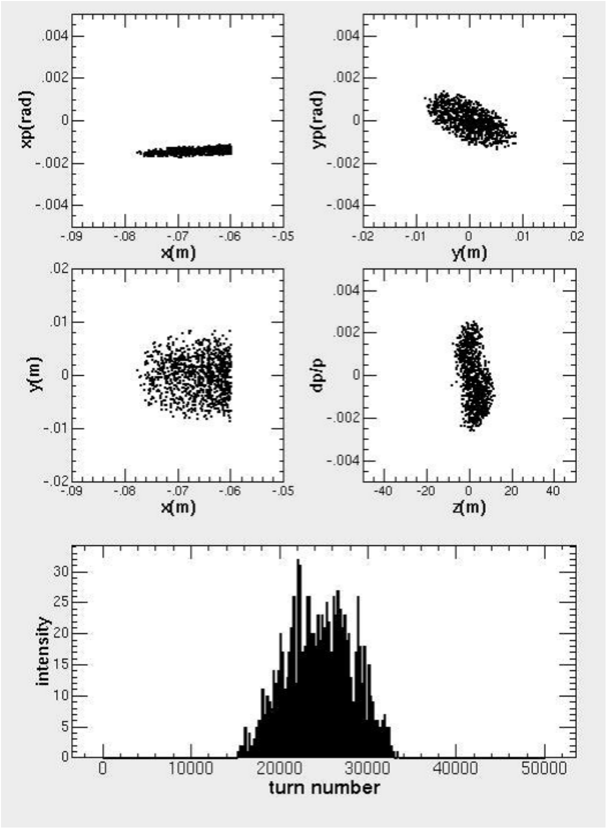

Figure 3.6: Simulations of the phase space distributions of the beam extracted from the MR.

### 3.3.1 Transport beam line hardware

In this section, the proton beam line hardware is described. Most of the hardware elements introduced in the proton beam transport line are of a conventional design, thus we do not need any special development except for the AC dipole magnet. Auxiliary components such as power supply and vacuum systems are also standard.

#### 3.3.1.1 Magnet system

Most of the beam transport line magnets will be shared with the high-momentum beam line and they are therefore required to be able to transport a proton beam of 30 GeV. The beam is bent in the NP hall to be transported onto the COMET target. For this bending we need a series of bending magnets probably with a C-shape to allow beam branching. An interlock system is necessary for radiation safety and needs to be designed to allow for different magnet excitation configurations such that the experimental area can be accessed both in the high momentum proton beam line and COMET beam line without shutting down the accelerator.

#### 3.3.1.2 Power supply system

The power supply system can be the same as those used in the A-line beam transport line. The necessary electricity and cooling water is estimated based on the specifications the A-line magnets.

#### 3.3.1.3 Vacuum system

Since we need to reduce beam loss and unexpected radiation doses, it is necessary to evacuate the transport line beam pipe. The required level of 0.1–1 Pa can be realized without any difficulty by installing scroll vacuum pumps at about every 20 m of the beam line. Oil-free scroll pumps will be used to prevent radiation-contaminated oil mist from being distributed in the environment.

# Chapter 4

# Muon Beam

## 4.1 Introduction

The muon beam line of COMET Phase-I will include the pion capture section and the muon transport section up to the end of first 90° bend of the COMET experiment. The design of the muon beam line of COMET Phase-I is identical to that of the full COMET experiment, and therefore the technical details of the pion capture section and muon transport section are not described in this document. We focus instead on features that are specific to COMET Phase-I, such as the beam configuration at the end of COMET Phase-I muon beam line. Figure 4.1 shows a schematic layout of the muon beam line and detector for COMET Phase-I.

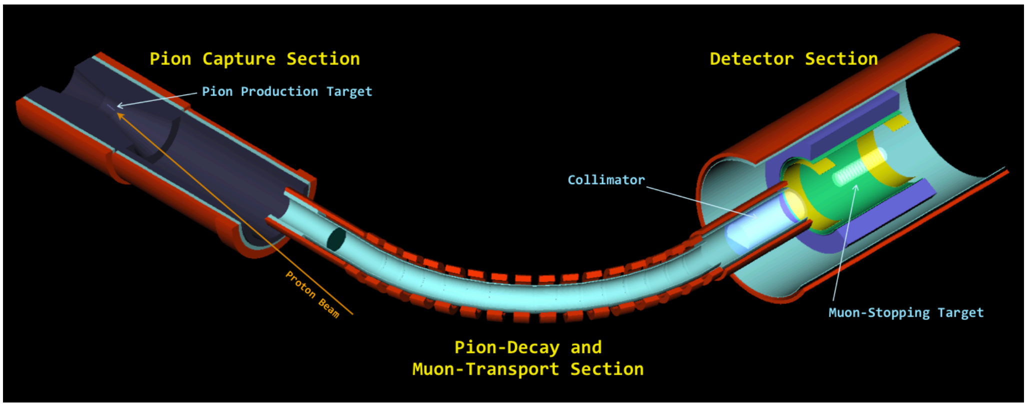

Figure 4.1: Schematic layout of the muon beam line for COMET Phase-I.

## 4.2 Muon Beam

COMET Phase-I uses negatively-charged low-energy muons, which can be easily stopped in a muon-stopping target. The low-energy muons are mostly produced by the decay in flight of low-energy pions. Therefore, the production of low-energy pions is of major interest. At the same time, high-energy pions, which could potentially cause background events, should be eliminated as well as possible.

Muons and pions are transported to the muon stopping target through the muon beam line, which consists of curved and straight superconducting solenoid magnets. The requirements for the muon beam line section are:

- the muon beam line should be long enough for low-energy pions to decay to muons,
- the muon beam line should have high transport efficiency for muons with a momentum of 40 MeV/$c$,
- the muon beam line should select low momentum negative muons and eliminate high momentum ($p_\mu > 75$ MeV/$c$) muon to avoid backgrounds from muon decays in flight.

At COMET Phase-I, we intend to construct the muon beam line at least up to the end of the first 90° bending section so that the muon beam can be extended beyond the concrete radiation shielding. It would be desirable to extend the muon beam line further if additional funds are available.

### 4.2.1 Beam optics of curved solenoids

Charge and momentum selection of beam particles can be performed using curved (toroidal) solenoids, which introduce dispersion into the beam. It is known that in a curved solenoid, the center of the helical trajectory of a charged particle drifts in a direction that is perpendicular to plane containing the curved solenoid. The magnitude of drift ($D$[m]) is given by

$$\begin{aligned} D &= \frac{1}{qB}\left(\frac{s}{R}\right)\frac{p_L^2+\frac{1}{2}p_T^2}{p_L}, & (4.1)\\ &= \frac{1}{qB}\left(\frac{s}{R}\right)\frac{p}{2}\left(\cos\theta+\frac{1}{\cos\theta}\right), & (4.2)\end{aligned}$$

where $q$ is the electric charge of the particle (including its sign), $B$ [T] is the magnetic field at the axis, and $s$ [m] and $R$ [m] are the path length and the radius of curvature of the curved solenoid, respectively. Here, $s/R(=\theta_{\rm bend})$ is the bending angle $\theta_{\rm bend}$ and $D$ is proportional to $\theta_{\rm bend}$, and $p_L$ and $p_T$ [GeV/$c$] are the longitudinal and transverse momenta, respectively. The pitch angle of the helical trajectory is represented by $\theta$. Charged particles with opposite signs drift in opposite directions. This can be used for charge and momentum selection if a suitable collimator is placed after the curved solenoid.

An additional vertical dipole field can be applied in order to maintain along the solenoidal axis the centers of the helical trajectories of the muons that have a specific momentum $p_0$. The magnitude of this compensating dipole field is given by

$$B_{\rm comp} = \frac{1}{qR}\frac{p_0}{2}\left(\cos\theta_0+\frac{1}{\cos\theta_0}\right), \qquad (4.3)$$

where the trajectories of negatively charged particles with momentum $p_0$ and pitch angle $\theta_0$ are corrected to be on-axis.

## 4.3 Muon Beam Simulation Study

A full Geant 4 based Monte Carlo simulation suite for COMET, called "COMET_G4", has been developed for studies of the muon beam and other components including the detector systems. COMET_G4 has been used to perform full-scale simulations of the muon beam.

The hadron production code, MARS, is used to provide input data for COMET_G4. Three-dimensional magnetic field distributions were calculated using TOSCA, taking account the geometry of each coil and the iron yokes.

## 4.4 Beam at the End of the First 90° Bend

The beam properties at the end of the first 90° bend are obtained using COMET_G4. At this location, a beam collimator is placed to eliminate particles that represent backgrounds to the $\mu^- - e^-$ conversion search.

### 4.4.1 Dispersion distribution

By the end of first 90° solenoid bend, the beam becomes dispersive. This momentum dispersion is very important and useful for eliminating high energy muons above 75 MeV/$c$, which would otherwise contribute to background events through their decay in flight. At the same time, it is useful to eliminate positively charged particles. Figure 4.2 shows histograms of momentum (namely, dispersion) vs. vertical position (Y) before the beam collimator for different correction dipole fields. It is noted that there are two numbers that represent the magnetic fields, corresponding to the different dipole fields which are superimposed on the fields of the first 90° bend and the second 90° bend respectively. For COMET Phase-I, only the first number is relevant.

### 4.4.2 Momentum distribution

Figure 4.3 shows the momentum distribution of the different types of particles at the end of the first 90° bend for a correction dipole field of 0.018T.

### 4.4.3 Time distribution

Figure 4.4 shows the time distributions of different charged particles in the muon beam, such as $\mu^-$s, $\pi^-$s, and $e^-$s before the collimator at the first 90° bend. The width is determined by different helical pitches of the muon trajectories. The time distribution of electrons is very sharp earlier in the pulse, however, followed by a small tail.

## 4.5 Beam at the Muon Stopping Target

Since the magnetic field at the detector (of 1 Tesla) is smaller than that at the muon beamline, the beam would spread when it enters the detector. The beam collimator is placed just after the end of the first 90° bend to determine a beam size so that muons that are not stopped in the muon stopping target are eliminated before entering the detector.

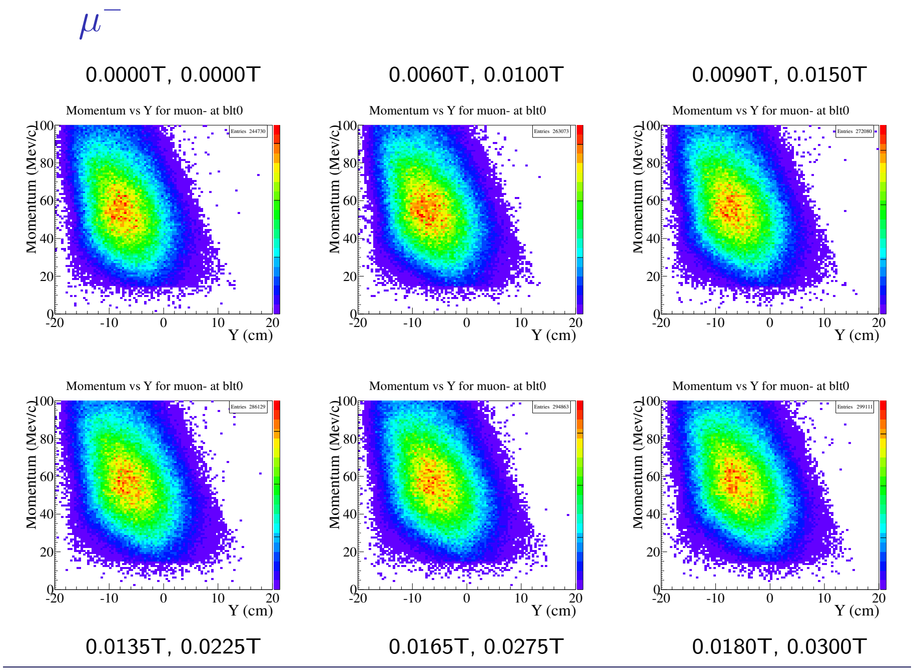

Figure 4.2: Dispersion of negative muons (momentum vs. vertical (Y) position) at the end of the first 90° bend for different correction dipole fields.

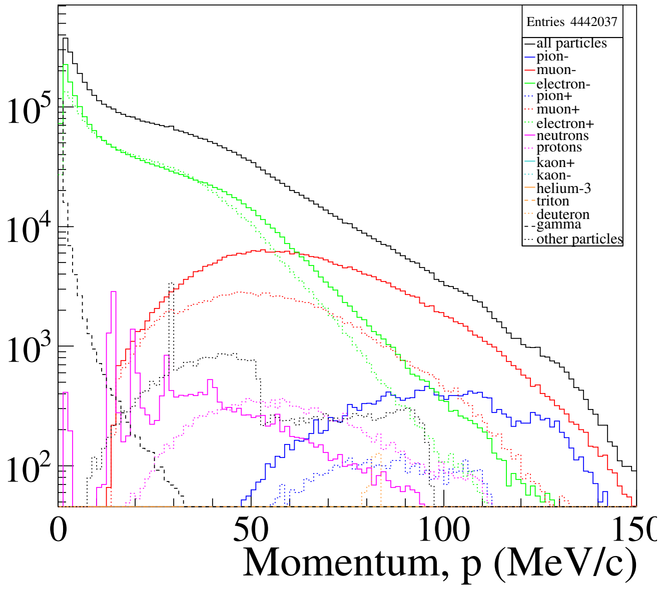

Figure 4.3: Momentum distribution of the different types of particles at the end of the first 90° bend for a correction dipole field of 0.018T.

And at the same time, it would eliminate high momentum muons of $P_\mu > 75$ MeV/$c$. The diameter of the collimator is 200 mm.

To do simulation studies, several virtual beam monitors were placed to examine beam profiles. Figure 4.5 shows those virtual beam monitors used in the present beam simulation

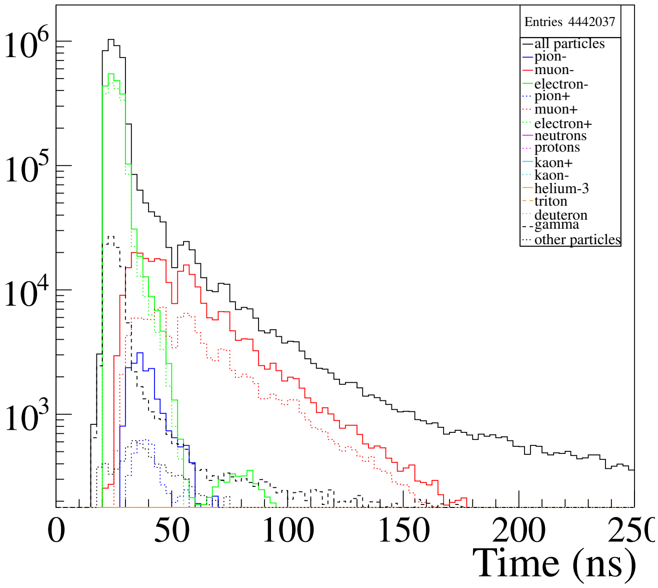

Figure 4.4: Arrival time distributions of various beam particles for the case of a correction dipole field of 0.018 T.

studies.

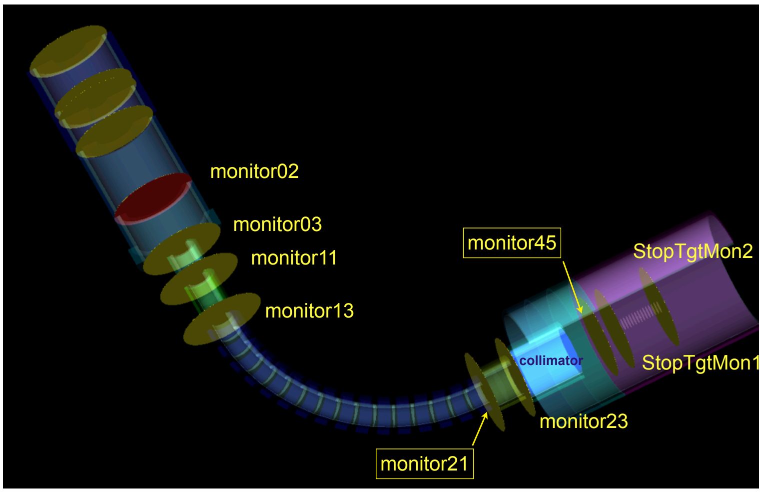

Figure 4.5: schematic layout of the muon beamline for COMET Phase-I and locations of virtual beam monitors.

The beam profiles of negative muons and negative pions before and after the beam collimator are presented in Figs. 4.6 and 4.7 respectively. In these figures, momentum distribution (left), dispersion of vertical position vs. momentum (middle), and timing distribution (right) are shown. It can be seen that the beam collimator is effective for the selection of a beam.

Figure 4.8 shows momentum distribution of negative muons coming to the muon stopping target and a faction of muons stopped in the muon stopping target. A fraction of

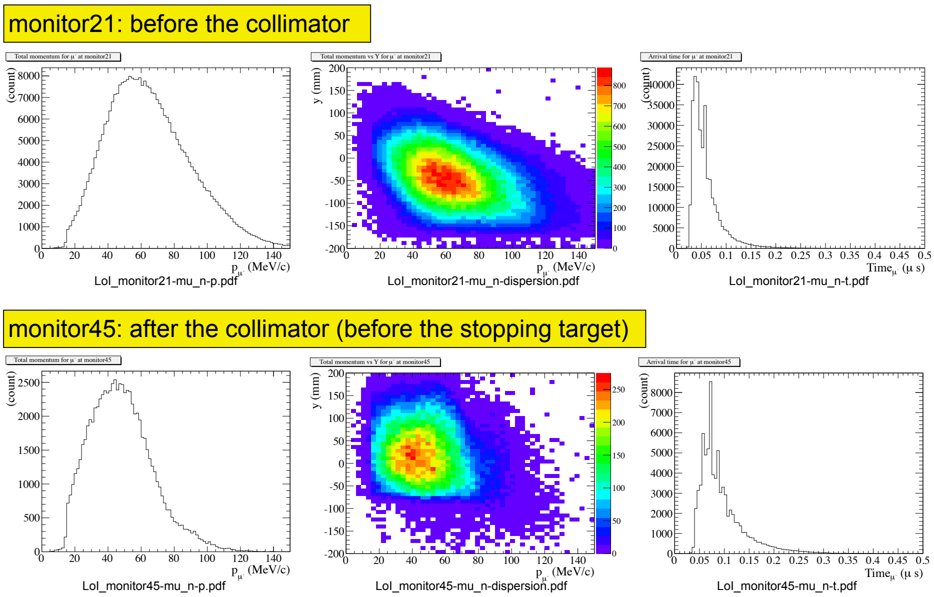

Figure 4.6: Profile of negative muons before and after the beam collimator.

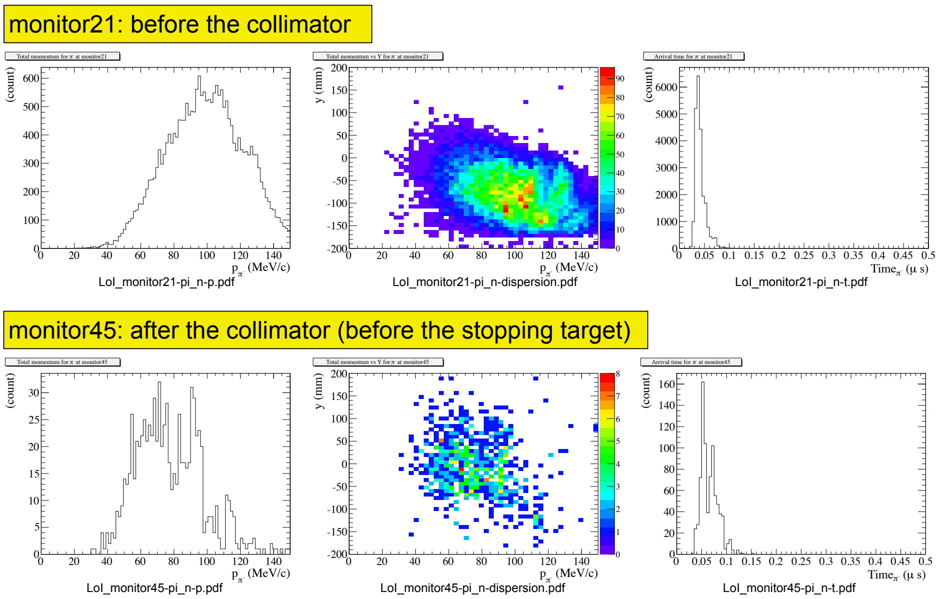

Figure 4.7: Profile of negative pions before and after the beam collimator.

the muon stopped is about 0.5. The numbers of particles coming to the muon stopping target (after the beam collimator) are summarized in Table 4.1.

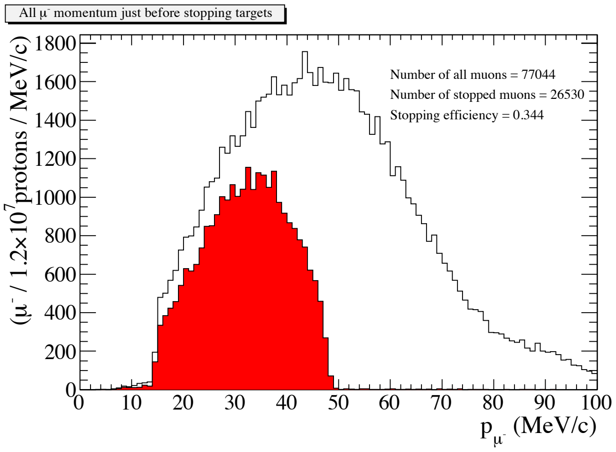

Figure 4.8: Momentum distribution of muons coming to the muon stopping target. The spectrum in red is a fraction of muons stopped in the muon stopping target.

Table 4.1: Numbers of different beam particles per proton at the muon stopping target.

| $\mu^-$ | | | $\pi^-$ |
|---|---|---|---|
| all | stopped | $P_\mu > 75$ MeV/$c$ | all |
| 0.0066 | 0.0023 | $5.7 \times 10^{-4}$ | $6.9 \times 10^{-5}$ |

# Chapter 5

# Detector

## 5.1 Introduction

In COMET Phase-I, we would like to

1. make a direct measurement of the proton beam extinction and other potential background sources for the full COMET experiment, using the actual COMET beamline; and
2. carry out a search for $\mu^-{-}e^-$ conversion with a sensitivity better than achieved by SINDRUM-2.

The detector configurations for the two goals mentioned above could be different, once they are optimized for their best performance. In the following, detector configurations for the two goals are described.

## 5.2 Detector for Background Measurements

The direct measurement of potential background sources will be vital for the COMET experiment. The current background estimates are made by extrapolating existing measurements over four orders of magnitude and uncertainties are therefore difficult to quantify and are potentially large. However, once the partial muon beamline is completed, realistic background estimations can be made from direct measurements. Based on these, the final design of the COMET beamline and detectors will be optimised and uncertainties on the background estimations minimized. This will significantly enhance the ultimate sensitivity of the COMET experiment.

Figure 5.1 shows a schematic view of the setup for background measurement. Measurement of the proton beam extinction ratio will be done by using segmented hodoscope counters as used in previous studies. The setup composed of a solenoid magnet with 0.85–1 T magnetic field strength, 5 layers of tracker, and crystal calorimeter. Detectors are located in a vacuum vessel functioning as a cryostat of the spectrometer magnet. The same detector technology as the COMET detector will be employed. The tracker will be constructed using straw chambers being developed for the COMET tracker. The crystal calorimeter will be composed of GSO or LYSO crystals; R&D is in progress and production will be ready in time for COMET Phase-I. We will make a decision which crystal to use according to the result of R&D. Performance of these detectors will be investigated

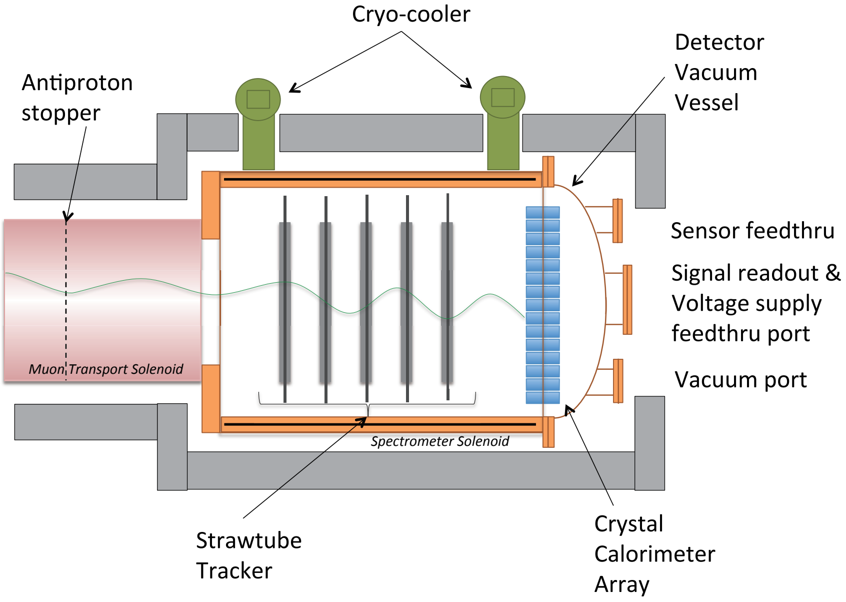

Figure 5.1: Setup for the background measurement in COMET Phase-I.

in this measurement and upgraded for the COMET experiment if necessary. It is also possible to test readout electronics and the data acquisition scheme. In this sense this setup will be a real prototype of the COMET detector.

The detector is required to provide sufficient information to identify particles in the beam and measure their momenta. Because charge selection is not performed in the Phase-I beam transport setup, all kind of particles are contained in the beam; p, $\overline{\mathrm{p}}$, $\mathrm{e}^{\pm}$, $\mu^{\pm}$, and $\pi^{\pm}$ ($\mathrm{K}^{\pm}$). These particles are identified mainly using $dE/dx$ information in the tracker and the ratio of energy and momentum ($E/p$). The momentum measurement is carried out by reconstructing the track using the tracker hits. The Kalman filter technique will be used for evaluating track momenta as is planned for the COMET experiment. Shower shape information in the calorimeter will be utilized for $\overline{\mathrm{p}}$ identification. The possibility to measure the direction of photons contained in the beam is under consideration. We expect that this can be carried out by inserting a converter between tracker layers. The configuration will be optimized with Monte Carlo simulation.

We need to reduce the primary proton intensity much below 1 kW to ensure safe detector operation. In addition proton beam extraction from the MR should be done in the normal slow extraction mode. This will help to reduce the detector occupancy rate, realizing reliable and stable measurements. The primary proton beam energy is supposed to be 8 GeV but measurement at higher energy will be made. The reason for a beam energy of 8 GeV is that the antiproton production cross section is known to rapidly increase above 8 GeV. We plan to investigate how the number of antiprotons is reduced by inserting a stopper in the beam line and what kind of possible background particles are emitted from it. Currently estimation of the number of antiprotons contained in the secondary beam for the final COMET configuration is done only with Monte Carlo simulation. Thus, a real measurement will certainly provide invaluable information. If the antiproton rate above 8 GeV stays in an acceptable range, we can use higher energy proton beam, which can provide a higher pion production rate and smaller beam emittance when the beam is extracted from the MR.

## 5.3 Detector Options to Search for $\mu^-{-}e^-$ Conversion

The search for $\mu^-{-}e^-$ conversion with a sensitivity beyond that achieved to date can be made. The pion contamination in the muon beam at COMET Phase-I will be high due to the shorter muon beamline. However, since the muon intensity will be the highest in the world by several orders of magnitude, as for the full COMET experiment, we will be able to probe beyond the current limit and set the world's best limit should no signal be observed.

Two types of detector configuration are considered for the $\mu^-{-}e^-$ conversion search in COMET Phase-I. One is a cylindrical detector option, and the other is a transverse tracker detector option, in which the detector for background measurements mentioned before is reused. The former is a detector dedicated for COMET Phase-I to maximize an experimental sensitivity for $\mu^-{-}e^-$ conversion search, and the latter is a prototype detector for the full COMET experiment.

## 5.4 Cylindrical Detector for $\mu^-{-}e^-$ Conversion Search

The baseline option for the detector to search for $\mu^-{-}e^-$ conversion is a cylindrical detector. Figure 5.2 shows a schematic view of the detector setup, where the tracking chamber surrounds cylindrically a muon-stopping target located at the center of the detector. A trigger counter is placed in front of the tracking chamber. Cherenkov hodoscopes are installed at the both ends of the detector for electron identification. The whole detector is placed in a large solenoid magnet of a magnetic field of 1 Tesla. An active cosmic-ray shielding is installed to the detector. To monitor a number of muons stopped in the muon stopping target, a detector to measure muonic X-rays is placed. The detector configuration is similar to the detector of SINDRUM II at PSI.

The cylindrical detector has several features as follows;

- To reduce background events, in particular electrons from muon decays in orbit and protons from nuclear muon capture, the requirement of minimum transverse momentum ($P_T$) can be placed. And in a cylindrical detector, the requirement can be easily determined by the radial location of the first layer of tracking chambers and a solenoid magnetic field.
- Most beam particles that do not stop in a muon-stopping target will go downstream and escape from the detector. The background rate is therefore reduced as well as the rate in the detector to be read out.

### 5.4.1 Drift chamber

The baseline option of tracking chamber is a drift gas chamber. The drift chamber covers from 545 mm to 805 mm in a radial direction. The length of the drift chamber is 1500

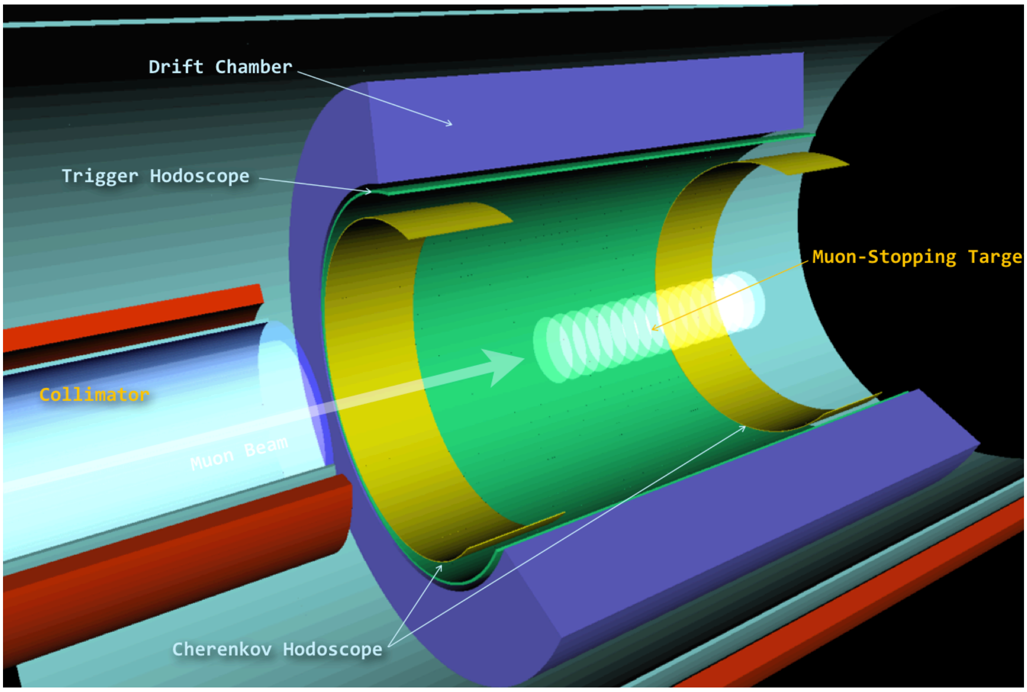

Figure 5.2: Schematic view of the cylindrical detector for $\mu^- - e^-$ conversion search.

mm long. It has 5 super-layers, and each super-layer has 5 sense wires. The 2nd and 4th super-layers are a stereo layer with a stereo angle of 3.5° and the 1st, 3rd and 5th layers are an axial layer. A sense wire is surrounded by a field wire, forming a drift cell of 1 $\mathrm{cm}^2$. A drift chamber gas is $\mathrm{Ar} : \mathrm{C_2H_6} = 50 : 50$. The inner and outer walls of the drift chamber is carbon fiber of 400 $\mu$m in thickness. The parameters of the drift chamber are summarized in Table 5.1.

Table 5.1: Parameters for COMET drift chamber

| parameter | value |
|---|---|
| inner radius | 545 mm |
| outer radius | 805 mm |
| # of super-layers | 5 |
| # of layers in super-layer | 5 |
| sense wire spacing | 10 mm |
| length | 1500 mm |

### 5.4.2 Trigger counter

The segmented trigger counter is placed before the drift chamber. For this purpose, a concentric layer consisting of segmented plastic scintillators is placed. This also provides trigger timing. As described in Section 5.4.4, the hit rate of the drift chamber is determined by protons emitted from nuclear muon capture. This also serves to reduce protons entering into the drift chamber.

### 5.4.3 Muon stopping target

The muon-stopping target is composed of 17 aluminum disks of 200 $\mu$m thickness with a distance between disks of 50 mm. This configuration is the same as for COMET. The target parameters are summarized in Table 5.2.

Table 5.2: Parameters of muon stopping target.

| parameter | value |
|---|---|
| target disk diameter | 200 mm |
| target disk thickness | 200 $\mu$m |
| number of target disks | 17 |
| spacing between disks | 50 mm |
| total length of target system | 800 mm |

### 5.4.4 Hit rates of tracking chamber

The available maximum muon beam intensity will be limited by the detector occupancy rate. As described before, charged particles with their transverse momentum ($P_T$) greater than 70 MeV/$c$ might reach the tracking chamber. There are several sources of such charged particles; (1) electrons from muon decays in orbit (DIO), (2) electron and positrons from high energy photon conversion, and (3) protons emitted from nuclear muon capture, namely $\mu^- + N \to N' + p + \nu_\mu$.

The hit rate due to the DIO electrons is estimated to be small and that due to proton emission dominates. Although there is no experimental data available for the rate of protons emitted after muon capture in aluminum, we can estimate the measured energy spectrum of charged particles emitted from muon capture in $^{28}$Si [40]. It is assumed that the proton emission probability per muon capture in aluminum is 0.15, as for the measurement for $^{28}$Si. It is noted that a theoretical estimation is 0.04 proton emission per muon capture in aluminum. Figure 5.3 shows an energy spectrum of protons emitted from nuclear muon capture on $^{28}$Si. [1]

To estimate single hit rates from proton emission, the energy spectrum emitted from muon capture is fit to an empirical function as follows [41].

$$P(T) = A\left(1 - \frac{T_{th}}{T}\right)^{\alpha} \exp^{-\frac{T}{T_0}} \tag{5.1}$$

where $T$ is a kinetic energy with the fitted parameters of $T_{th} = 1.4$ MeV, $\alpha = 1.328$ and $T_0 = 3.1$ MeV, and $A$ is a normalization parameter. In our Monte Carlo simulation, protons are generated isotropically based on Eq. (5.1). The trigger counters are cylindrical and are located at a radial position of 500 mm from the beam axis. The simulations were

---

[1] The COMET collaboration is planning to measure the proton emission rate from muon capture in aluminum either at TRIUMF or at PSI by using their DC muon beam, together with the Mu2e group.

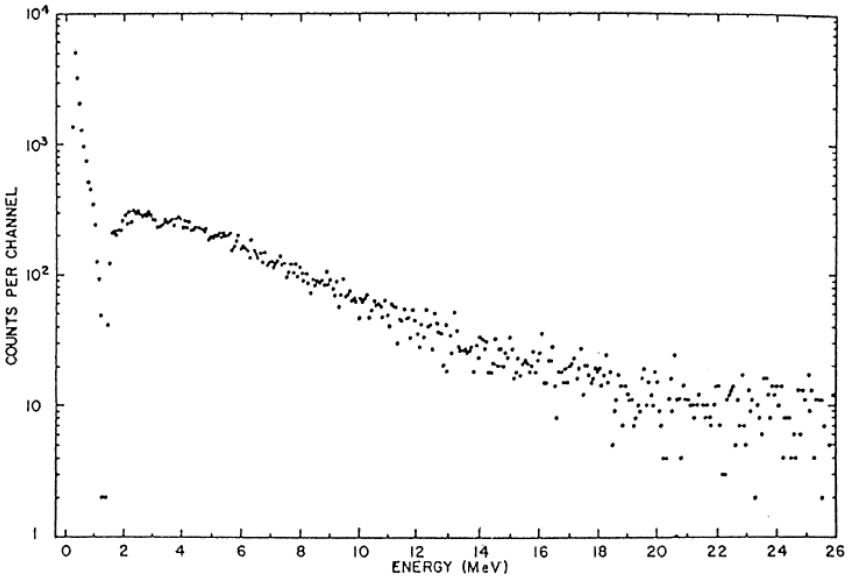

Figure 5.3: Energy spectrum of protons emitted from nuclear muon capture on Si.

done with three different thickness of trigger counters, namely 0 mm, 5 mm, and 7.5 mm. It is also noted that some large fraction of protons stop in the muon-stopping target made of aluminum. Figure 5.4 shows a proton momentum spectrum generated (larger than 50 MeV/$c$) in the simulation study, and regions in red show protons reaching the first layer. The results are shown in Table 5.3, where the proton emission rate of 0.15 per muon capture is assumed.

Table 5.3: Total numbers of hits in the first layer by protons emitted from muon capture for different trigger counter thickness. 100 k proton events were generated.

| trigger counter thickness | 0 mm | 5 mm | 7.5 mm |
|---|---|---|---|
| number of 1 hit events | 2467 | 87 | 28 |
| number of 2 hit events | 73 | 8 | 1 |
| number of 3 hit events | 9 | 0 | 0 |
| number of 4 hit events | 1 | 0 | 0 |
| sum of hits | 2644 | 103 | 30 |
| hits per proton emission | 2.6 % | 0.1 % | 0.03 % |
| hits per muon capture* | $3.9 \times 10^{-3}$ | $1.5 \times 10^{-4}$ | $4.5 \times 10^{-5}$ |

* 15 % protons per muon capture is assumed.

If we assume the number of muons stopped in the muon-stopping target is $5.8 \times 10^9$/s, the number of muon capture on aluminum is about $3.5 \times 10^9$/s since the fraction of muon capture in aluminum is $f_{cap} = 0.61$. Therefore the total number of hits in all the cells in the first layer is estimated to be $5.3 \times 10^5$/s $(= (1.5 \times 10^{-4}) \times (3.5 \times 10^9))$ for the case of a trigger counter of 5 mm thickness. The total number of cells in the first layer

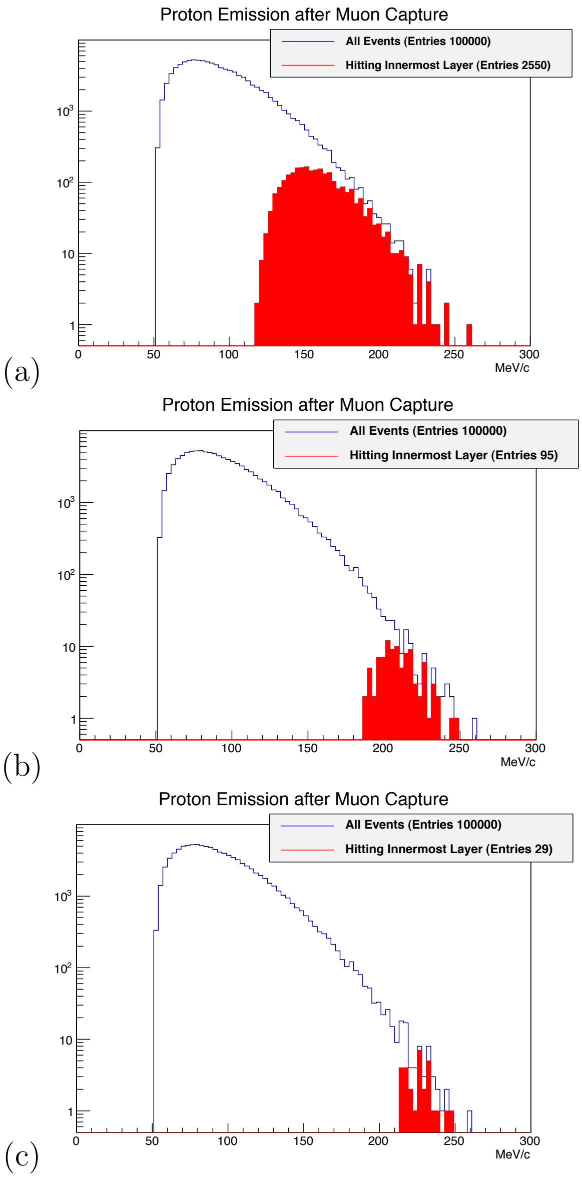

Figure 5.4: Proton momentum spectra generated in simulation studies. The region in red shows the protons reaching the drift chamber after penetrating through the trigger counter: (a) no trigger counter, (b) a 5-mm thick absorber, (c) a 7.5-mm thick absorber.

of the drift chamber will be about 345. Therefore, the hit rate per drift chamber wire will be about 1.5 kHz. This rate is well below the limit of stable operation region of a gas detector. And since the rate of proton emission follows a muon lifetime in a muonic atom, this single rate becomes lower in the time window of the measurement. And this can work as a trigger counter as well.

### 5.4.5 Requirement of momentum resolutions

Momentum resolution of the drift chamber is critical to discriminate the $\mu^-{-}e^-$ conversion signals from electrons from DIO. The end point of the DIO spectrum approaches the energy of the $\mu^-{-}e^-$ conversion signal, although it falls off quickly, being proportional to $(\Delta E)^5$ where $\Delta E = E_{\mu-e} - E_{\rm DIO}$, $E_{\mu-e}$ is the energy of $\mu^- - e^-$ conversion electron, and $E_{\rm DIO}$ is an energy of the DIO electron. For aluminum, $E_{\mu-e}$ is 104.9 MeV. The DIO electron energy spectrum has been calculated for the muonic aluminum [42]. Figure 5.5 shows the DIO spectrum for muonic aluminum atom. The energy difference of $\Delta E = 1.5$ MeV is seen at a sensitivity of $10^{-15}$.

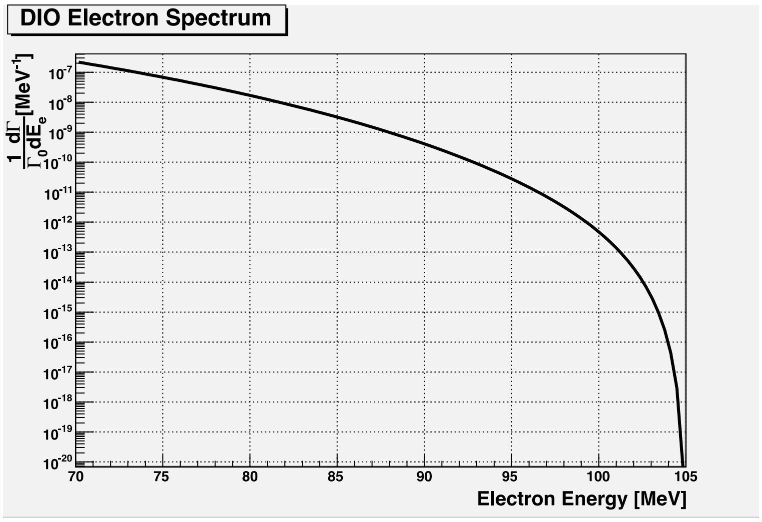

Figure 5.5: Energy spectrum of electrons from muon DIO from muonic aluminum

### 5.4.6 Tracking simulation studies

Tracking performance was studied by using Geant-3 Monte Carlo simulation. In this simulation, electrons of 105 MeV/$c$ leaving the stopping target were generated isotropically from 17 disks of aluminum of 200 $\mu$m. The drift chamber wall was taken into account and a gas of Ar:$C_2H_6$=50:50 was filled inside the chamber volume.

The hit information generated from the Geant-3 simulation is smeared by the expected position resolutions of the drfit chamber. They are $\Delta x = \Delta y = 100$ $\mu$m and $\Delta z = 2$ mm. The hit positions thus obtained after smearing were used for track reconstruction.

Track reconstruction was performed by "Genfit"[43] with "GeaneTrackRep2" as a track follower, which uses the Kalman filter to take account of multiple scattering in tracking materials. In Genfit, to find a good track it is required for the number of reconstructed hits to be more than four and for the normalized $\chi^2$ to be less than five. Figure 5.6 shows an example of reconstructed event displays, where it can be seen that a track loses its energy after passing the trigger counter.

The intrinsic momentum resolution is evaluated from the residual distribution of true momentum and reconstructed momentum. It is shown in Figure 5.7.

### 5.4.7 Distribution of reconstructed momentum

The fitted momentum could be lower than the true momentum of 105 MeV/$c$ since electrons lose their energy in the muon stopping target and the trigger counter. This energy loss would reduce the peak of the momentum distribution and also it would produce a

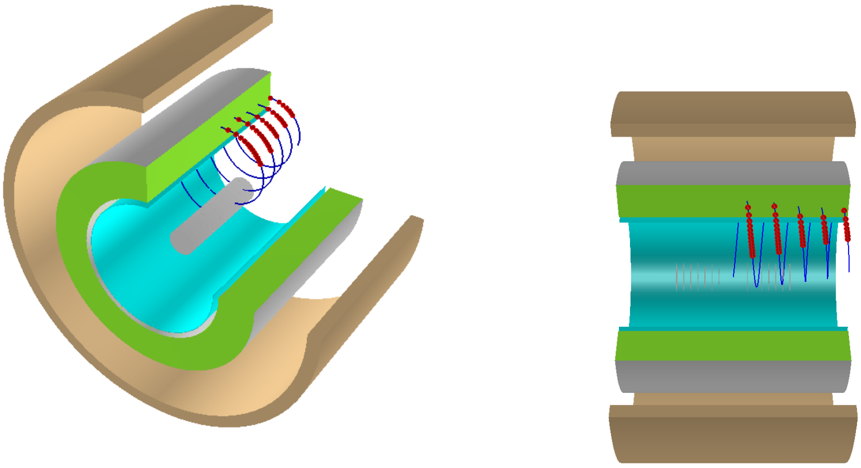

Figure 5.6: Event displays of the cylindrical detector. A view from 45 degree (top) and a side view (bottom). A typical track is shown. The green section shows layers of drift chambers. The brown section shows superconducting magnet coil. The blue line shows a reconstructed track of a 105 MeV/$c$ electron.

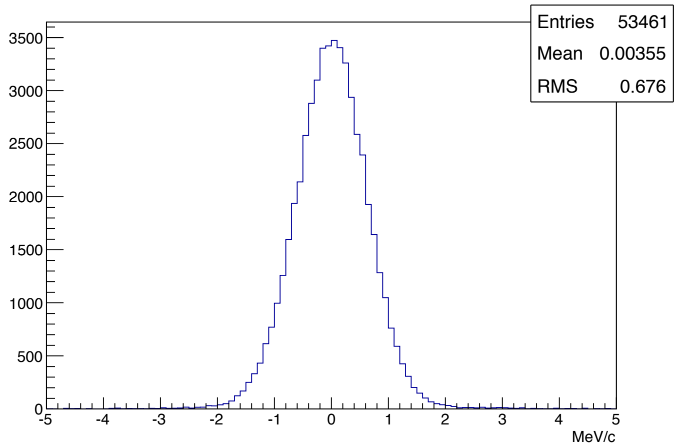

Figure 5.7: Intrinsic momentum resolution of the drift chamber.

low-energy tail and broaden the core peak width owing to energy straggling. Figure 5.8 shows the reconstructed momentum resolutions for (a) no trigger counter, (b) with a 5 mm thick trigger counter, and (c) with a 7.5 mm thick trigger counter. The distribution of reconstructed momentum is important to discriminate the $\mu^-{-}e^-$ conversion events from the electrons from DIO. The capability of discrimination will be discussed in Chapter 6. However, the obtained distribution indicates a search sensitivity of less than $10^{-14}$.

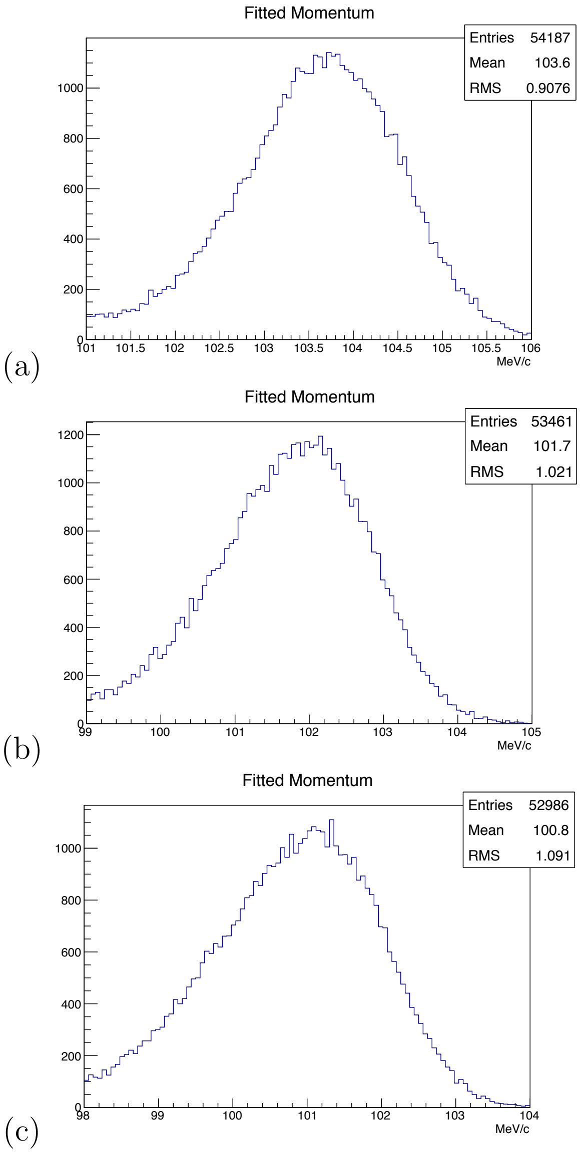

Figure 5.8: Reconstructed momentum distribution for 105 MeV/c electrons (a) no absorber, (b) 5 mm trigger counter, and (c) 7.5 mm trigger counter.

## 5.5 Transverse Tracker Detector for $\mu^{-}$–$e^{-}$ Conversion Search

This option re-utilizes the setup for background measurement shown in Figure 5.1. A cylindrical muon-stopping target composed of 11 aluminum disks with 5 cm spacing is located near the exit of the muon transport solenoid. Muons that are not stopped in the target and high momentum electrons emitted from muon decay in flight are prevented from entering the detector by a beam blocker located behind the target. Two wedges to stop the high momentum protons emitted after muon capture are located between the target and detector. Those are fixed on the inner surface of the spectrometer magnet. The tracker is composed of 5 layers of straw tube trackers followed by a crystal calorimeter to measure the electron energy. The calorimeter is expected also to provide a timing signal to reject prompt background and to measure drift length in the tracker. A schematic view of the setup together with signal momentum tracks are shown in Figure 5.9. Acceptance to the signal event is estimated to be $22.5 \pm 1.5\%$ by generating 105 MeV/c electrons at the center of 1st and last target disks and taking a mean of transmission probabilities.

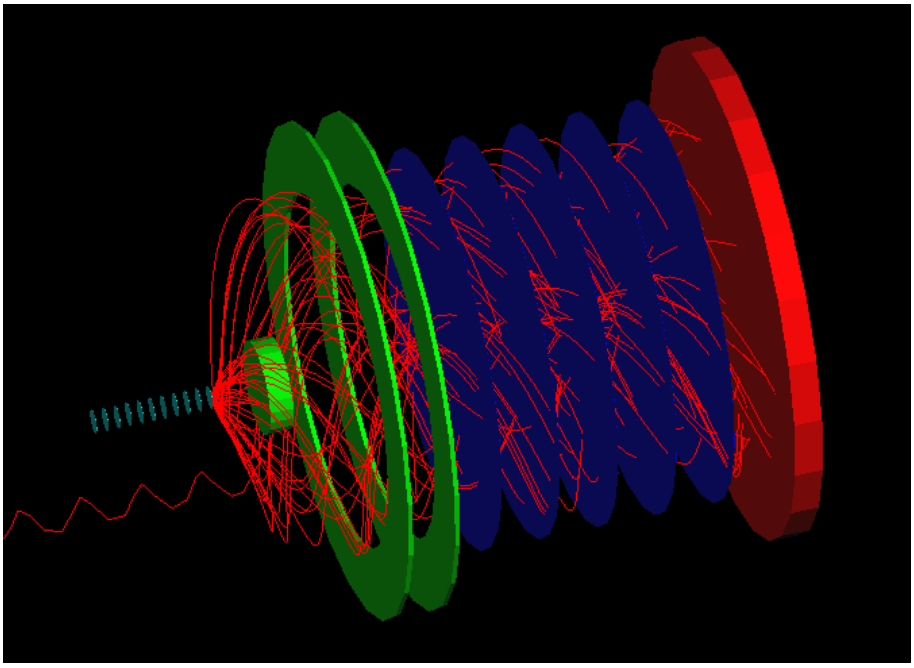

Figure 5.9: Schematic view of the transverse tracker detector with 5 layers of straw tube trackers (blue) and calorimeter (red). Superimposed are 105 MeV/c electron tracks generated in the last target disk. The beam blocker and two wedges to stop protons with high transverse momenta are shown in green.

High momentum protons emitted after muon capture are blocked by the blocker when emitted in forward direction, and stopped by the wedges when emitted with large transverse momentum. On the other hand low momentum protons, dominating the charged particle spectrum emitted after muon captures, cannot be reduced efficiently by either of these. To remove these protons we locate a degrader of 500 $\mu$m thickness 150 mm downstream of the target. The degrader works to eliminate low-momentum protons producing enormous amount of hits in the 1st layer of the tracker. These protons carry kinetic energy as small as 4 MeV and thus can be easily removed by a thin foil without deteriorating the momentum resolution of signal electrons. The momentum spread of signal electrons caused by the degrader is estimated to be 200 MeV/c in FWHM.

Detector hit rate is estimated in a similar way as done for the cylindrical detector. If we use 200 straw chambers in the front-most layer, the hit rate will be 80 kHz for $5 \times 10^9$ muon stops per second. This is sufficiently small for stable detector operation.

The momentum resolution of the spectrometer is expected to be as good as that of the COMET detector (1.0% in sigma) since almost the same detector configuration is employed.

# Chapter 6

# Signal Sensitivity and Backgrounds

## 6.1 Introduction

In this chapter, the signal sensitivity, and the expected background events in the COMET Phase-I search for $\mu^{-}-e^{-}$ conversion are evaluated. To estimate the experimental sensitivity, a 0.4 $\mu$A proton beam at 8 GeV, yielding a total beam power of 3.2 kW, is assumed. It corresponds to about $2.5 \times 10^{12}$ protons per second. A nominal running time of $10^{6}$ s (about 12 days), gives a total of $2.5 \times 10^{18}$ protons on target.

## 6.2 Signal Sensitivity for $\mu^{-}-e^{-}$ Conversion

As described in Chapter 5, we are considering two detector options to search for $\mu^{-}-e^{-}$ conversion at COMET Phase-I. One is a cylindrical detector as the baseline design, and the other is a transverse tracker detector. In the following, the estimations of signal sensitivity for each option are described.

### 6.2.1 Signal acceptance for cylindrical detector

The acceptance for $\mu^{-}-e^{-}$ conversion signals is determined by several factors. They are the

- geometrical acceptance including a solid angle of the detector,
- efficiency of track reconstruction with track quality cuts,
- efficiency of momentum selection (a momentum window cut),
- efficiency of timing selection (a timing window cut), and
- efficiency of event trigger and a DAQ live time.

The geometrical acceptance depends on the detector configuration such as the size and radial positions of the tracking components. In the present design, charged particles with momenta less than 70 MeV/$c$ do not reach the tracking chamber. Figure 6.1 shows the distributions of transverse momenta ($P_T$) and longitudinal momenta ($P_L$) for the generated events (in black) and reconstructed events (in blue) of 105 MeV/$c$ electrons. From this it is found that a $P_T$ threshold of about 80 MeV/$c$ is obtained, with an acceptance of about 40%, as determined by the geometrical solid angle.

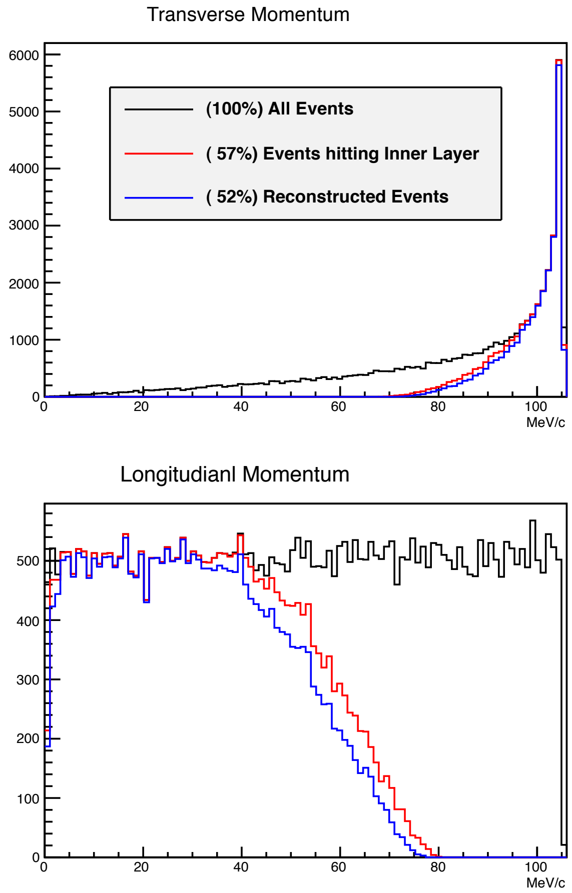

Figure 6.1: Distributions of transverse momentum ($P_T$) for generated events (black) and reconstructed events (blue). The comparison of these gives the geometrical acceptance. This is the case for trigger counters of 5 mm thickness.

A momentum cut can be used to reduce contamination from DIO electrons. Figure 6.2 shows the reconstructed momentum spectrum of $\mu^-{-}e^-$ conversion signal events that were generated using Monte Carlo simulations and the DIO electron spectrum. In Fig. 6.2, the vertical scale is normalized so that the integrated area of the signal event curve is one event, assuming a branching ratio of $B(\mu N \to eN) = 3 \times 10^{-15}$. A detailed description of the estimation of contamination from DIO electrons is presented in Section 6.3.1.1. In this study, the range of the momentum cuts is determined in such a way that a contamination from DIO electrons of 0.05 events is expected for a single event sensitivity of $\mu^-{-}e^-$ conversion of $3 \times 10^{-15}$. Table 6.1 shows the momentum cut and its signal acceptance for different thicknesses of the trigger counter.

The efficiencies of the timing selection and the trigger and DAQ are assumed to be the same as those in the COMET CDR. From these, the net acceptance for the $\mu^-{-}e^-$ conversion signal, $A_{\mu\text{-}e} = 0.1$, is obtained for the case of a trigger counter of 5 mm thickness. The breakdown of the acceptance is shown in Table 6.2.

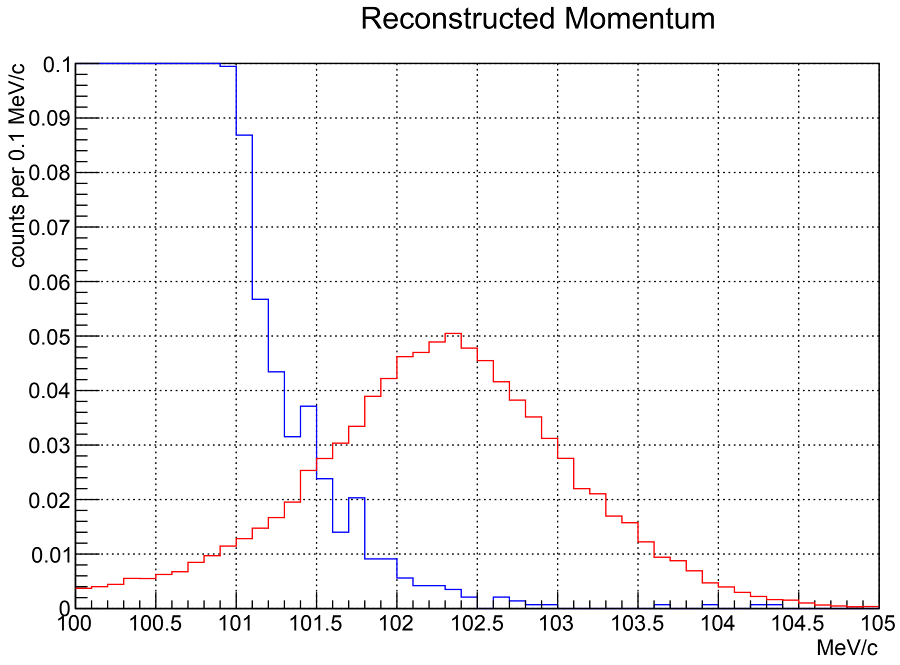

Figure 6.2: Distributions of reconstructed $\mu^- - e^-$ conversion signals and reconstructed DIO events for the case of trigger counter of 5 mm thickness. The vertical scale is normalized so that the integrated area of the signal is equal to one event with its branching ratio of $B(\mu N \to eN) = 3 \times 10^{-15}$. The momentum cut of 101.9 MeV/$c$ is used in this report.

Table 6.1: Momentum cut values and their efficiencies for different thickness of trigger counters. The net efficiency below is the product of the geometrical acceptance and the efficiency of the momentum cut.

| trigger counter | geometrical & tracking | momentum threshold | momentum cut | net efficiency |
|---|---|---|---|---|
| no | 41 % | $P_e > 103.5$ MeV/$c$ | 70 % | 29 % |
| 5 mm | 40 % | $P_e >$101.9 MeV/$c$ | 66 % | 26 % |
| 7.5 mm | 38 % | $P_e > 100.4$ MeV/$c$ | 55 % | 21 % |

### 6.2.2 Signal sensitivity for cylindrical detector

The single event sensitivity is given by

$$B(\mu^- + \mathrm{Al} \to e^- + \mathrm{Al}) \quad = \quad \frac{1}{N_\mu^{\mathrm{stop}} \cdot f_{\mathrm{cap}} \cdot A_{\mu\text{-}e}}\,, \tag{6.1}$$

where $N_\mu^{\mathrm{stop}}$ is the number of muons stopping in the muon target, $f_{\mathrm{cap}}$ is the fraction of muon capture and $A_{\mu\text{-}e} = 0.09$ is the signal acceptance. The fraction of muon capture for aluminum is $f_{\mathrm{cap}} = 0.61$.

By assuming a proton beam of 8 GeV with 0.4 $\mu$A, a total beam power is about

Table 6.2: Breakdown of the $\mu^-{-}e^-$ conversion signal acceptance per stopped muon for the case of trigger counters of 5 mm thickness.

| Event selection | Value | Comments |
|---|---|---|
| Geometrical acceptance | 0.40 | tracking efficiency included |
| Momentum selection | 0.66 | $P_e >$101.9 MeV/$c$ |
| Timing selection | 0.39 | same as COMET |
| Trigger and DAQ | 0.9 | same as COMET |
| Total | 0.09 | |

3.2 kW. A proton current of 0.4 $\mu$A corresponds to $2.5 \times 10^{12}$ protons/s. With a running period of $10^6$ s, a total number of protons on target is about $2.5 \times 10^{18}$.

A number of muons stopped at the muon stopping target is estimated to be 0.0023 per proton from the COMET_G4 simulation program, as mentioned in Chapter 4. From these, a total number of muon stopped of $N_\mu^{stop} = 5.8 \times 10^{15}$ ($= 0.0023 \times 2.5 \times 10^{18}$) is obtained. It corresponds to $5.8 \times 10^9$ muons stopped/s.

By using these numbers thus obtained, from Eq.(6.1), the single event sensitivity is given by

$$B(\mu^- + \mathrm{Al} \to e^- + \mathrm{Al}) = 3.1 \times 10^{-15}. \tag{6.2}$$

The 90 % confidence upper limit is given by

$$B(\mu^- + \mathrm{Al} \to e^- + \mathrm{Al}) < 7.2 \times 10^{-15}. \tag{6.3}$$

### 6.2.3 Transverse tracker detector option

The transverse tracker detector may have less geometrical coverage since the detector can detect only events coming into the downstream hemisphere. Detailed simulation studies to estimate geometrical acceptance will be made soon, together with tracking efficiencies.

## 6.3 Background Estimations for $\mu^-{-}e^-$ Conversion

As in the Conceptual Design Report (CDR) of COMET [37], potential backgrounds sources for the search for $\mu^-{-}e^-$ conversion are grouped into four categories.

1. intrinsic physics backgrounds,
2. beam-related prompt backgrounds,
3. beam-related decayed backgrounds, and
4. other backgrounds including cosmic ray backgrounds.

A list of background events are summarized in Table 6.3. They are evaluated for COMET Phase-I as follows.

Table 6.3: A list of potential backgrounds for a search for $\mu^-$–$e^-$ conversion.

| | |
|---|---|
| Intrinsic physics backgrounds | |
| Muon decay in orbit | Bound muons decay in a muonic atom |
| Radiative muon capture (external) | $\mu^- + A \rightarrow \nu_\mu + A'$, $A' \rightarrow \gamma + A$,<br>followed by $\gamma \rightarrow e^- + e^+$ |
| Radiative muon capture (internal) | $\mu^- + A \rightarrow \nu_\mu + A'$, $A' \rightarrow e^+ + e^- + A$, |
| Neutron emission after after $\mu^-$ capture | $\mu^- + A \rightarrow \nu_\mu + A'$, $A' \rightarrow n + A$,<br>and neutrons produce $e^-$ |
| Charged particle emission after $\mu^-$ capture | $\mu^- + A \rightarrow \nu_\mu + A'$,<br>$A' \rightarrow p$ (or $d$ or $\alpha$) $+A$<br>followed by $p$ (or $d$ or $\alpha$) produce $e^-$ |
| Beam related prompt backgrounds | |
| Radiative pion capture (external) | $\pi^- + A \rightarrow \gamma + A'$<br>followed by $\gamma \rightarrow e^- + e^+$ |
| Radiative pion capture (internal) | $\pi^- + A \rightarrow e^+ + e^- + A'$ |
| Beam electrons | $e^-$ scattering off a muon stopping target |
| Muon decay in flight | $\mu^-$ decays in flight to produce $e^-$ |
| Pion decay in flight | $\pi^-$ decays in flight to produce $e^-$ |
| Neutron induced backgrounds | neutrons hit material to produce $e^-$ |
| Beam related delayed backgrounds | |
| Delayed-pion radiative capture | $\pi^- + A \rightarrow \gamma + A'$, $\gamma \rightarrow e^- + e^+$ |
| $\overline{p}$ induced backgrounds | $\overline{p}$ hits material to produce $e^-$ |
| Other backgrounds | |
| Cosmic-ray induced backgrounds | |
| False tracking | |

### 6.3.1 Intrinsic physics backgrounds

Negative muons stopped in material are immediately trapped by the Coulomb potential of the nucleus of the material, and fall down to the 1S orbit of a muonic atom. There are two major allowed processes in which a bound $\mu^-$ could proceed. They are

- muon decays in orbit (DIO), and
- nuclear muon capture (NMC).

#### 6.3.1.1 Muon decays in orbit

Muon DIO is a Michel decay, $\mu^- \rightarrow e^- \nu_\mu \overline{\nu}_e$, of the muons that are bound in a muonic atom under a Coulomb potential of the nucleus. Because of the recoil of the nucleus, an electron from the Michel decay can be boosted. The maximum energy of the $e^-$ exceeds the end point energy of the ordinary Michel decay of 52.8 MeV and extends to the momentum range of the $\mu^-$–$e^-$ conversion signal. This is one of the dominant background sources.

The momentum spectrum of electrons from muon decay in orbit for aluminum can be calculated based on the model described in [42]. Figure 5.5 shows the momentum spectrum of DIO electrons from aluminum. Based on the calculated spectrum, DIO electrons are generated in a Monte Carlo simulation and their tracks are reconstructed with Genfit. Fig. 6.2 shows the reconstructed momentum spectrum of DIO electrons with $\mu^- - e^-$ conversion signals for the trigger counter of 5 mm thickness.

This momentum spectrum is then integrated above the momentum threshold of the $\mu^- - e^-$ conversion signal region. Figure 6.3 shows the integrated fraction of DIO events as a function of momentum threshold, and the fraction of $\mu^- - e^-$ conversion signal events,. The momentum threshold of the $\mu^- - e^-$ conversion signal region is determined so that the fraction of DIO electrons is 0.05 events. For this case of the trigger counter of 5 mm thickness, the lower momentum threshold is determined to be 101.9 MeV/$c$.

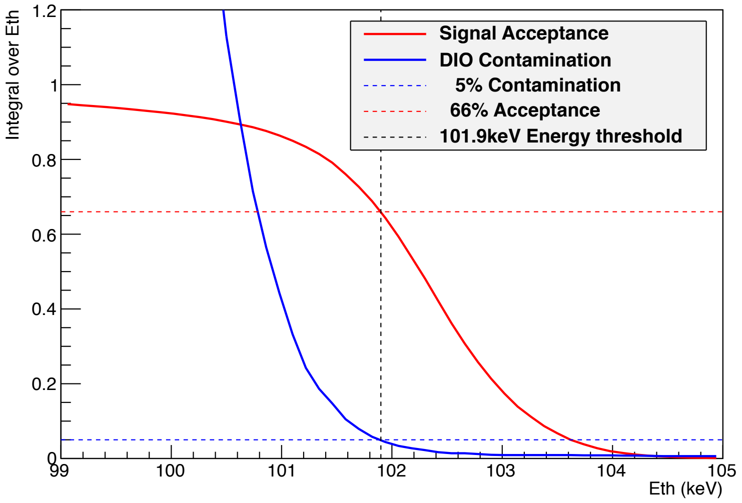

Figure 6.3: Event fractions for DIO electron events and $\mu^- - e^-$ conversion events as a function of lower momentum threshold of the signal region. This is the case for trigger counter of 5 mm.

### 6.3.2 Beam-related prompt backgrounds

The beam-related prompt backgrounds arise from protons between the beam pulses. These backgrounds are suppressed by the proton beam extinction.

#### 6.3.2.1 Radiative pion capture

The radiative pion capture (RPC) background is caused by pions that contaminate the muon beam. These pions are produced in primary proton interactions with the pion production target and can be transported to the muon stopping target.

The RPC background events can be estimated as

$$\begin{aligned} N_{\mathrm{RPC}} &= N_p \times R_{\mathrm{extinction}} \times R_{\pi-\mathrm{stop}/p} \times \\ &\quad P_{\mathrm{RPC}} \times P_{\gamma-e^-} \times A_{\mathrm{geometry}} \times A_{\mathrm{tracking}} \, , \end{aligned} \tag{6.4}$$

where $N_p$ is a total number of protons on the pion production target, $R_{\mathrm{extinction}}$ is a proton beam extinction factor, $R_{\pi-\mathrm{stop}/p}$ is a number of $\pi^-$s coming to a muon stopping target per proton, and number of initial protons, $P_{\rm RPC}$ is a branching ratio of radiative muon capture, $P_{\gamma-e^-}$ is a probability of conversion of the RPC photon to an electron of 105 MeV/$c$, $A_{\rm geometry}$ is a detector acceptance of the RPC-originated electrons of 105 MeV/$c$, $A_{\rm tracking}$ is an efficiency of tracking.

From the COMET Phase-I beam simulation, $R_{\pi-{\rm stop}/p} = 6.9 \times 10^{-5}$ at the target position, as shown in Section 4. The stopping fraction of pions is about 0.9. The branching ratio of radiative pion capture, $P_{\rm RPC}$, is known to be about 2 %. $P_{\gamma-e^-} = 1.4 \times 10^{-5}$ is the same as the COMET experiment. The product $A_{\rm geometry} \times A_{\rm tracking} = 0.28$ is obtained from the COMET Phase-I simulation studies. The original value of $R_{\rm extinction}$ in the COMET CDR is $10^{-9}$. From our experimental measurements at the J-PARC MR, this is expected to be much less than $10^{-9}$, however we assume the conservative value of $R_{\rm extinction} = 10^{-9}$ here. [1] With $N_P = 2.5 \times 10^{18}$ protons on target, a total of 0.012 background events from the external conversion of radiative pion capture is obtained. The contribution of internal conversion is about the same as that of external conversion. Therefore, $N_{\rm RPC} = 0.024$ events is estimated with a proton beam extinction factor of $10^{-9}$.

#### 6.3.2.2 Muon decay in flight

Muons decaying in flight can produce energetic electrons that have a total momentum (of about $p_{\rm total} > 102$ MeV/$c$) and transverse momentum (of about $p_T > 50$ MeV/$c$). For the decay electrons to have $p_{\rm total} > 102$ MeV/$c$, the muon momentum must exceed 75 MeV/$c$ ($p_\mu > 75$ MeV/$c$). A Monte Carlo simulation has been done to estimate the yield of muons of $p_\mu > 75$ MeV/$c$ that are transported through the muon beam line and enter the target region, giving a value of about $5.7 \times 10^{-4}$. The probability for muons to decay in flight in the muon beam line is about $3 \times 10^{-2}$. The probability of having an electron energy of 103 MeV/$c < p_{total} <$ 105 MeV/$c$, and $p_T > 50$ MeV/$c$ is less than $10^{-8}$. With a beam extinction factor of $10^{-9}$, the total background level from muon decay in flight is less than 0.0004.

#### 6.3.2.3 Other beam related backgrounds

The other beam related backgrounds are (1) beam electrons, (2) pion decay in flight and (3) neutron induced backgrounds. The contributions from these sources of background are expected to be very similar to the case of the full COMET experiment. While detailed studies will follow, here we assume the same estimated backgrounds rates between the two phases of COMET.

### 6.3.3 Beam related prompt backgrounds

The beam related prompt background events are also expected to be the same for both the COMET Phase-I and the full COMET.

### 6.3.4 Cosmic ray induced backgrounds

The background events induced by cosmic rays are proportional to the total running time. The running time of COMET Phase-I is short, at $10^6$ sec, in comparison to that of the full

---

[1] The proton extinction factor of $10^{-10}$ is required for the Mu2e experiment at FNAL.

Table 6.4: Summary of estimated background events for a single-event sensitivity of $3 \times 10^{-15}$ with a proton extinction factor of $10^{-9}$

| Background | estimated events |
|---|---|
| Muon decay in orbit | 0.05 |
| Radiative muon capture | $< 0.001$ |
| Neutron emission after muon capture | $< 0.001$ |
| Charged particle emission after muon capture | $< 0.001$ |
| Radiative pion capture | 0.024 |
| Beam electrons | $< 01$ |
| Muon decay in flight | 0.0004 |
| Pion decay in flight | $< 0.0001$ |
| Neutron induced background | 0.024 |
| Delayed radiative pion capture | 0.002 |
| Anti-proton induced backgrounds | 0.007 |
| Cosmic ray muons | 0.0001 |
| Electrons from cosmic ray muons | 0.0001 |
| Total | 0.11 |

COMET of $2 \times 10^7$ sec. Therefore, the estimated background events are about a factor of 20 less than that of the full COMET experiment.

### 6.3.5 Summary of background estimations

Table 6.4 shows a summary of the estimated backgrounds. The total estimated background is about 0.11 events for a single event sensitivity of $3.1 \times 10^{-15}$ with a proton extinction factor of $10^{-9}$. If the proton extinction factor is increased, the expected background events are further reduced.

# Chapter 7

# Infrastructure

This chapter describes the necessary infrastructure for COMET Phase-I. To start up the experiment promptly and derive valuable results, we propose the construction of the proton beamline, pion production and collection system, muon transport solenoid up to first 90 degree bend, proton beam dump, and the experimental area as a J-PARC facility. Construction will be a in cooperative effort between the facility and the experimental collaboration. It is important to deal with necessary utilities such as electricity and cooling water to cover future upgrades of the experiment.

## 7.1 Primary Proton Beam line

Figure 7.1 shows a schematic of the proposed beam line configuration. The primary proton beam for COMET Phase-I is extracted from the MR and transported through the beam switch yard area. In the switch yard area a new primary line (B line, shown in orange in Figure 7.1) will be branched from the existing primary line (A line). The B line is used to transport the primary beam both to the high-momentum beam line (shown in yellow in Figure 7.1) and the COMET beamline (shown in orange in Figure 7.1). A switching magnet will be installed to control the beam destination between the high-momentum beam line and COMET beam line. The COMET beam line will transport and focus the 8 GeV pulsed proton beam onto the pion production target located in the COMET Experimental hall. The high-momentum beam line, COMET beam line, and the upstream primary line that is shared by these two lines will be newly constructed in the medium term together with their beam dumps.

## 7.2 Experimental Area

The existing beam line is located 6.2 m below ground level, and the COMET beam line will be constructed at the same height. This means that the experimental area needs to accommodate this configuration for the set-up to be installed at the same height. The ground floor space of the experimental area will be used for utility installations such as a helium compressor, refrigerator, cooling tower, and magnet power supplies. Access areas will be prepared to install equipment on the beam line floor. Necessary equipment for controlling and monitoring apparatus should be located in the vicinity of this. We plan to construct an upper floor for this purpose. Figure 7.2 shows a conceptual view of the beam

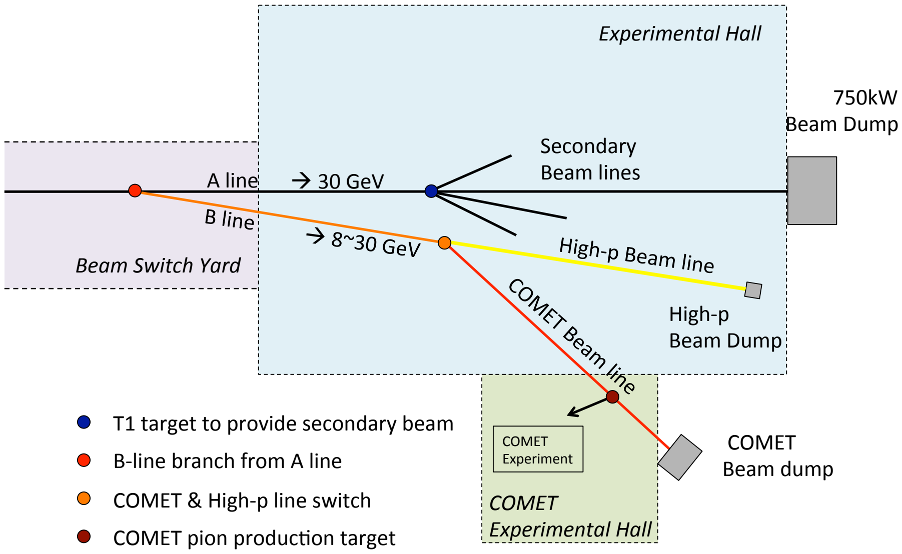

Figure 7.1: Schematic view of the primary beam line in the nuclear and particle physics experimental hall. A new primary beam line, B line shown in orange, will be branched from the existing A line. High-momentum beamline shown in yellow and COMET beam line shown in orange will share the upstream primary line.

line floor and COMET experimental hall. The experimental hall building is composed of three floors.

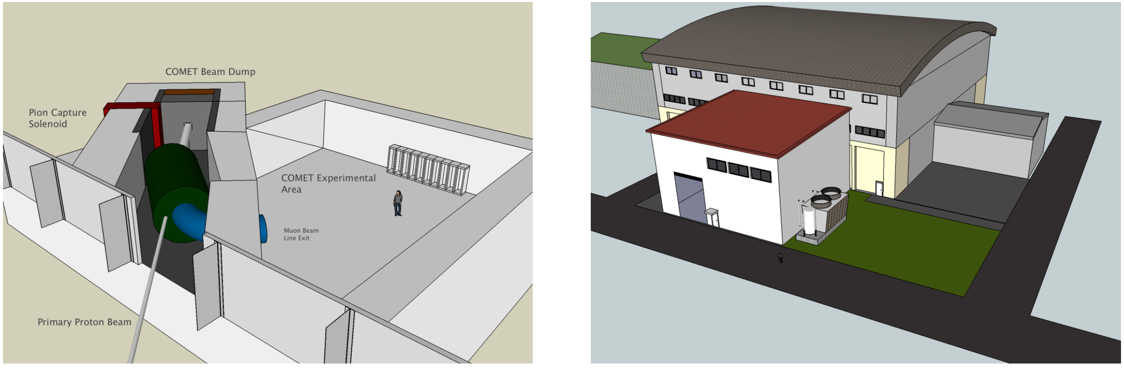

Figure 7.2: Conceptual view of the COMET beam line floor (left) and experimental hall building (right). The building will be constructed as an annex of the existing hall building.

## 7.3 Electricity and Cooling Water

We estimate here the necessary electricity for the proton beam transport magnets, the pion capture solenoid and its refrigerator, the muon transport solenoid, the detector solenoid,

Table 7.1: Power requirements. External extinction devices and GM-type refrigerators will not be installed in COMET Phase-I but are included here considering the possibility of upgrades in the future.

| Equipment | Power (MW) |
|---|---:|
| Beam transport magnets | 0.2 |
| External extinction devices | 0.2 |
| Solenoid magnets | 0.12 |
| He refrigerator | 0.12 |
| GM-type refrigerators | 0.2 |
| Vacuum pumps | 0.1 |
| Detectors Electronics | $< 0.02$ |
| DAQ system | $< 0.02$ |
| Frontend computers | $< 0.02$ |
| Total | 1.0 |

Table 7.2: Cooling water requirements. The requirements for GM-type refrigerators are included for as they will be needed in any future upgrades.

| Equipment | Cooling water ($\ell$/min) |
|---|---:|
| Magnets and extinction devices | 400 |
| Helium refrigerator compressor | 120 |
| GM-type refrigerator compressors | 100 |

and the detector components. In Phase-I, only a part of muon transport solenoid is constructed and no spectrometer curved solenoid; however considering future upgrades we provide estimates for all possible configuration options for the future. In addition to this, as described in COMET CDR, the COMET experiment may need to install an external-extinction device for improving the beam extinction factor. In these estimates, the necessary electricity for external beam extinction is also included. Table 7.1 summarizes the estimated required electric power. In total 1.0 MW is needed to power the full configuration.

Cooling water is needed for the beam line magnets and related equipment and the helium refrigerator compressor for supplying liquid helium to the solenoid magnet. As in the case of electricity, cooling water for GM-type refrigerators is included as this will be needed in a future upgrade. Table 7.2 summarizes the necessary amount of cooling water. Here we assume a cooling water temperature of 20-25 °C.

# Chapter 8

# Cost and Schedule

## 8.1 Cost

Table 8.1 summarizes the cost estimate required to initiate COMET Phase-I. We expect that the budget request for the J-PARC mid-term plan will cover the building for the COMET experimental hall, the primary proton beam and its beam dump, the pion capture solenoid and muon transport solenoid magnets, radiation shielding for 3 kW operation, and beam line installation. We are also expecting the J-PARC project budget further to complete installations. We will likely be able to reuse existing equipment such as power supplies for the superconducting magnets and a refrigerator system to maximise cost reductions. The proton beam line magnets that were used at the KEK 12-GeV synchrotron will be also reused, but it may be that new magnets will be necessary for higher-power operation. The detector will be constructed with funding external to KEK. The experimental group will secure the financial resources needed for the detector.

## 8.2 Schedule

The technically-driven schedule for COMET Phase-I is shown in Table 8.1. Currently we are expecting to start construction in 2013, first by starting superconducting wire production, which is estimated to take one year. Technical design work of superconducting magnets will proceed to allow the timely start of construction after wire production. Magnet construction is estimated to take two years including all necessary testing, followed by installation and engineering runs on-site. The construction of the experimental area be started early in Japanese fiscal year (JFY) 2013 and be completed in JFY 2015. The beam line construction schedule is expected not to conflict with the operation of other beam lines. The construction schedule for the high-momentum beam line is an important consideration. Currently this is scheduled for JFY 2015–2016. As explained in the previous section, detector constructions is dependent on external funding outside KEK and is not guaranteed yet. However we plan to construct all components to be ready in time for the start of the experimental engineering run scheduled in JFY 2016.

Table 8.1: Cost estimate for COMET Phase-I in Oku (= $10^8$) Japanese yen. Additional funding is required to upgrade to the final COMET Phase-II configuration.

| | | Budget request | KEK internal | External funding | Optional | Future funding | Comments |
|---|---|---|---|---|---|---|---|
| Building | | 8.0 | | | | | |
| Beam dump | | 1.0 | 0.5 | | | | |
| SC magnet | | 8.0 | | | | | to first $90^o$ bend |
| | | | | | | 20.0 | remaining beam line |
| | W shield | | | | | 2.0 | for higher power |
| Power supply | | | | | 2.0 | | if purchased |
| | | | 0.5 | | | | installation |
| | | | | | | 2.5 | for upgrade |
| refrigerator | | | | | 2.0 | | if constructed |
| | | | 0.5 | | | | installation |
| Beam line | magnet | | 0.5 | | | | installation |
| | | | | | | 5.0 | for higher power |
| | piping | 0.3 | 0.3 | | | | |
| | cabling | 0.6 | 0.6 | | | | |
| | vacuum | 0.6 | 0.6 | | | | |
| Radiation shielding | NP-hall | 1.5 | | | | | for 3 kW operation |
| | | | | | | 6.5 | for high power |
| Safety | | | 0.5 | | | | |
| $\pi$ target | | | | 0.8 | | | experimental group |
| Detector | magnet | | 0.5 | 0.5 | | | for Phase-I |
| | $\mu$ target | | | 0.1 | | | experimental group |
| | $\mu$ monitor | | | 1.5 | | | experimental group |
| | tracker | | | 1.1 | | | experimental group |
| | ECAL | | | 1.6 | | | experimental group |
| | CR veto | | | 5.7 | | | experimental group |
| | DAQ | | | 0.5 | | | experimental group |
| Total | | 20.0 | 4.5 | 11.8 | 4.0 | 36.0 | 72.3+4.0 |

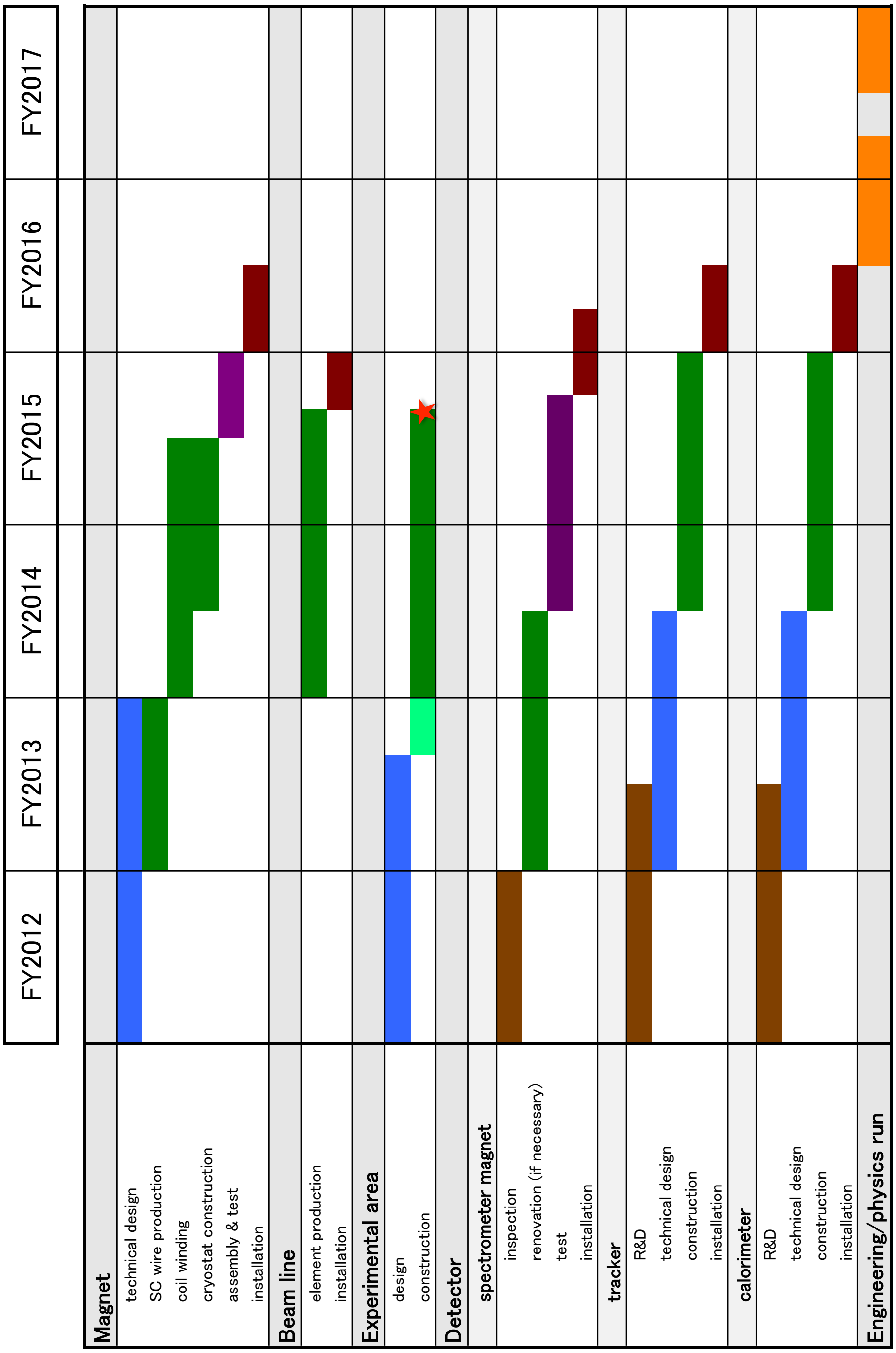

Figure 8.1: Technically-driven schedule for COMET Phase-I.

# Chapter 9

# Summary

This Letter of Intent (LoI) presents the staged approach of the construction of the COherent Muon to Electron Transition (COMET) experiment to search for coherent neutrinoless conversion of muons to electrons ($\mu^-{-}e^-$ conversion).

To realize this staged approach, we would like to construct the COMET proton beamline and the COMET muon beamline up to the end of the first 90° bend so that a muon beam can be extracted to the experimental area of the J-PARC NP experimental hall. This initial stage is called "COMET Phase-I" in this LoI.

Firstly with COMET Phase-I, we would like to make a direct measurement of the proton beam extinction and other potential background sources for the full COMET experiment, using the actual COMET beamline. The direct measurement of potential background sources will be vital for the COMET experiment. The current background estimates are made by extrapolating existing measurements over four orders of magnitude and uncertainties are therefore difficult to quantify and are potentially large. However, once the partial muon beamline is completed, it will be possible to make realistic background estimations using direct measurements. Based on these, the final design of the COMET beamline and detectors will be optimized and uncertainties on the background estimations minimized. This will significantly enhance the ultimate sensitivity of the COMET experiment.

Secondly, we would like to carry out a search for $\mu^-{-}e^-$ conversion with a singe-event sensitivity of better than $3.1 \times 10^{-15}$ which is a factor of 200 better than achieved by SINDRUM-II. Ultimately, with the completion of the rest of COMET beamline and detector, we intend to carry out the full COMET experiment (COMET Phase-II) to achieve a single-event sensitivity of $3 \times 10^{-17}$. Additionally, there is physics potential at COMET Phase-I to carry out other important CLFV searches, such as $\mu^- + Al \to e^+ + Na$ and $\mu^- + e^- \to e^- + e^-$ in a muonic atom. The proposed staged approach will produce valuable scientific outcomes *at each phase* and the physics impact of our CLFV search in COMET Phase-I will be significant.

In summary, we believe that the physics case made by the staged approach that is presented here for building the COMET experiment is extremely strong, and that it is aligned with the proposed J-PARC mid-term plan for the construction of the COMET beamline. We are hoping to start construction in 2013 and carry out measurements in 2016.

# Bibliography

[1] W. Bertl *et al.*, “A search for $\mu$-e conversion in muonic gold,” *The European Physical Journal C - Particles and Fields* **47** (2006) 337–346. http://dx.doi.org/10.1140/epjc/s2006-02582-x. 10.1140/epjc/s2006-02582-x.

[2] **MEGA Collaboration**, M. L. Brooks *et al.*, “New Limit for the Lepton-Family-Number Nonconserving Decay $\mu^+ \to e^+\gamma$,” *Phys. Rev. Lett.* **83** (Aug, 1999) 1521–1524. http://link.aps.org/doi/10.1103/PhysRevLett.83.1521.

[3] U. Bellgardt *et al.*, “Search for the decay $\mu^+ \to \mathrm{e}^+\mathrm{e}^+\mathrm{e}$,” *Nuclear Physics B* **299** no. 1, (1988) 1 – 6. http://www.sciencedirect.com/science/article/pii/0550321388904622.

[4] W. P, “Design of dynamic collimator for J-PARC Main Ring,” in *Proceedings of the First International Symposium on Lepton and Baryon Number Violation.* 1998.

[5] L. Willmann *et al.*, “New Bounds from a Search for Muonium to Antimuonium Conversion,” *Phys. Rev. Lett.* **82** (Jan, 1999) 49–52. http://link.aps.org/doi/10.1103/PhysRevLett.82.49.

[6] **Belle Collaboration**, K. Hayasaka *et al.*, “New search for $\tau \to \mu\gamma$ and $\tau \to \mathrm{e}\gamma$ decays at Belle,” *Physics Letters B* **666** no. 1, (2008) 16 – 22. http://www.sciencedirect.com/science/article/pii/S0370269308007673.

[7] **Belle Collaboration**, K. Abe *et al.*, “Upper Bound on the Decay $\tau \to \mu\gamma$ from the Belle Detector,” *Phys. Rev. Lett.* **92** (Apr, 2004) 171802. http://link.aps.org/doi/10.1103/PhysRevLett.92.171802.

[8] **BABAR Collaboration**, B. Aubert *et al.*, “Search for Lepton-Flavor Violation in the Decay $\tau^- \to \ell^-\ell^+\ell^-$,” *Phys. Rev. Lett.* **92** (Mar, 2004) 121801. http://link.aps.org/doi/10.1103/PhysRevLett.92.121801.

[9] P. Krolak *et al.*, “A Limit on the lepton family number violating process $\pi^0 \to \mu^\pm\mathrm{e}^\mp$. FNAL-799 experiment,” *Phys. Lett.* **B320** (1994) 407–410.

[10] **BNL**, D. Ambrose *et al.*, “New Limit on Muon and Electron Lepton Number Violation from $K^0_L \to \mu^\pm e^\mp$ Decay,” *Phys. Rev. Lett.* **81** (1998) 5734–5737, `arXiv:hep-ex/9811038`.

[11] A. M. Lee *et al.*, “Improved limit on the branching ratio of $K^+ \to \pi^+\mu^+\mathrm{e}^-$,” *Phys. Rev. Lett.* **64** (Jan, 1990) 165–168. http://link.aps.org/doi/10.1103/PhysRevLett.64.165.

[12] K. Arisaka *et al.*, “Search for the lepton-family number violating decays $K_L \to \pi^0 \mu^\pm \mathrm{e}^\mp$,” *Phys. Lett.* **B432** (1998) 230–234.

[13] R. Akers *et al.*, “Measurement of the $\tau^- \to h^- h^+ h^- \nu_\tau$ and $\tau^- \to h^- h^+ h^- \geq 1\pi^0 \nu_\tau$ branching ratios,” *Zeitschrift fr Physik C Particles and Fields* **68** (1995) 555–567. http://dx.doi.org/10.1007/BF01565256. 10.1007/BF01565256.

[14] P. Abreu et al., “Search for lepton flavour number violating $\mathrm{Z}^0$-decays,” *Zeitschrift fr Physik C Particles and Fields* **73** (1997) 243–251. http://dx.doi.org/10.1007/s002880050313. 10.1007/s002880050313.

[15] **Super-Kamiokande Collaboration**, Y. Fukuda *et al.*, “Evidence for Oscillation of Atmospheric Neutrinos,” *Phys. Rev. Lett.* **81** (Aug, 1998) 1562–1567. http://link.aps.org/doi/10.1103/PhysRevLett.81.1562.

[16] **Super-Kamiokande Collaboration**, S. Fukuda *et al.*, “Constraints on Neutrino Oscillations Using 1258 Days of Super-Kamiokande Solar Neutrino Data,” *Phys. Rev. Lett.* **86** (Jun, 2001) 5656–5660. http://link.aps.org/doi/10.1103/PhysRevLett.86.5656.

[17] T.-P. Cheng and L.-F. Li, “Muon-number-nonconservation effects in a gauge theory with $V + A$ currents and heavy neutral leptons,” *Phys. Rev. D* **16** (Sep, 1977) 1425–1443. http://link.aps.org/doi/10.1103/PhysRevD.16.1425.

[18] B. W. Lee and R. E. Shrock, “Natural suppression of symmetry violation in gauge theories: Muon- and electron-lepton-number nonconservation,” *Phys. Rev. D* **16** (Sep, 1977) 1444–1473. http://link.aps.org/doi/10.1103/PhysRevD.16.1444.

[19] S. Petcov, “The Processes $\mu \to \mathrm{e}\gamma, \mu \to \mathrm{e} + \mathrm{e} + \bar{\mathrm{e}}, \nu' \to \nu + \gamma$ in the Weinberg-Salam Model with Neutrino Mixing,” *Sov.J.Nucl.Phys.* **25** (1977) 340.

[20] W. Marciano and A. Sanda, “Exotic decays of the muon and heavy leptons in gauge theories,” *Physics Letters B* **67** no. 3, (1977) 303 – 305. http://www.sciencedirect.com/science/article/pii/037026937790377X.

[21] Z. Maki, M. Nakagawa, and S. Sakata, “Remarks on the unified model of elementary particles,” *Prog.Theor.Phys.* **28** (1962) 870–880.

[22] S. Glashow, J. Iliopoulos, and L. Maiani, “Weak Interactions with Lepton-Hadron Symmetry,” *Phys.Rev.* **D2** (1970) 1285–1292.

[23] O. U. Shanker, “HIGH-ENERGY ELECTRONS FROM BOUND MUON DECAY,” *Phys.Rev.* **D25** (1982) 1847.

[24] R. Watanabe, M. Fukui, H. Ohtsubo, and M. Morita, “ANGULAR DISTRIBUTION OF ELECTRONS IN BOUND MUON DECAY,” *Prog.Theor.Phys.* **78** (1987) 114–122.

[25] D. Bryman, M. Blecher, K. Gotow, and R. Powers, “Search for the reaction $\mu^- + \mathrm{Cu} \to \mathrm{e}^+ + \mathrm{Co}$,” *Phys.Rev.Lett.* **28** (1972) 1469–1471.

[26] A. Badertscher, K. Borer, G. Czapek, A. Fluckiger, H. Hanni, *et al.*, "A SEARCH FOR MUON - ELECTRON AND MUON - POSITRON CONVERSION IN SULFUR," *Nucl.Phys.* **A377** (1982) 406.

[27] D. Bryman, E. Clifford, M. Leitch, I. Navon, T. Numao, *et al.*, "SEARCH FOR mu e CONVERSION IN Ti," *Phys.Rev.Lett.* **55** (1985) 465.

[28] S. Ahmad, G. Azuelos, M. Blecher, D. Bryman, R. Burnham, *et al.*, "SEARCH FOR MUON - ELECTRON AND MUON - POSITRON CONVERSION," *Phys.Rev.* **D38** (1988) 2102.

[29] **SINDRUM II Collaboration.**, C. Dohmen *et al.*, "Test of lepton flavor conservation in $\mu \to$ e conversion on titanium," *Phys.Lett.* **B317** (1993) 631–636.

[30] **SINDRUM II Collaboration**, W. Honecker *et al.*, "Improved limit on the branching ratio of $\mu \to$ e conversion on lead," *Phys.Rev.Lett.* **76** (1996) 200–203.

[31] **MECO Collaboration**, Bachman M, "A Search for $\mu^- N \to e^- N$ with Sensitivity Below $10^{-16}$, **M**uon – **E**lectron **CO**nversion," *a research proposal to Brookhaven National Laboratory AGS* .

[32] **Mu2e collaboration**, "Proposal to Search for $\mu^- + N \to e^- N$ with a Single Event Sensitivity Below $10^{-16}$ (Mu2e Experiment)," *a research proposal to Fermilab* (2008) .

[33] K. Babu and R. Mohapatra, "New vector - scalar contributions to neutrinoless double beta decay and constraints on R-parity violation," *Phys.Rev.Lett.* **75** (1995) 2276–2279, `arXiv:hep-ph/9506354 [hep-ph]`.

[34] **SINDRUM II Collaboration**, J. Kaulard *et al.*, "Improved limit on the branching ratio of $\mu^- \to$ e$^+$ conversion on titanium," *Phys.Lett.* **B422** (1998) 334–338.

[35] M. Koike, Y. Kuno, J. Sato, and M. Yamanaka, "A new idea to search for charged lepton flavor violation using a muonic atom," *Phys.Rev.Lett.* **105** (2010) 121601, `arXiv:1003.1578 [hep-ph]`.

[36] T. Shibata and Y. Futo, "Production cross-section of antiprotons for the study of cosmic-ray propagation in the galaxy," *Astropart.Phys.* **29** (2008) 30–41.

[37] **COMET**, Y. G. Cui *et al.*, "Conceptual design report for experimental search for lepton flavor violating $\mu^- \to e^-$ conversion at sensitivity of $10^{-16}$ with a slow-extracted bunched proton beam (COMET),". KEK-2009-10.

[38] Ikegami M, "181 MeV acceleration at J-PARC LINAC," *High Energy Physics News, JAHEP* **25-4** (2007) 177–189.

[39] M. Tomizawa *et al.*, "Design of dynamic collimator for J-PARC Main Ring," in *PAC07, Albuquerque, New Mexico, USA*. 2007.

[40] S. E. Sobottka and E. L. Wills, "Energy Spectrum of Charged Particles Emitted Following Muon Capture in $\mathrm{Si}^{28}$," *Phys. Rev. Lett.* **20** (Mar, 1968) 596–598. http://link.aps.org/doi/10.1103/PhysRevLett.20.596.

[41] Hungerford E. V., "Comment on proton emission after muon capture," *MECO Technical Note 034* .

[42] A. Czarnecki, X. Garcia i Tormo, and W. J. Marciano, "Muon decay in orbit: Spectrum of high-energy electrons," *Phys. Rev. D* **84** (Jul, 2011) 013006. http://link.aps.org/doi/10.1103/PhysRevD.84.013006.

[43] C. Hoeppner, S. Neubert, B. Ketzer, and S. Paul, "A novel generic framework for track fitting in complex detector systems," *Nuclear Instruments and Methods in Physics Research Section A: Accelerators, Spectrometers, Detectors and Associated Equipment* **620** no. 23, (2010) 518 – 525. http://www.sciencedirect.com/science/article/pii/S0168900210007473.